The Astrophysical Journal Supplement Series, 122:299–329, 1999 May

FINAL ASTRO-2 CALIBRATION OF THE HOPKINS ULTRAVIOLET TELESCOPE

Jeffrey W. Kruk,[1] Thomas M. Brown,[1,2] Arthur F. Davidsen,[1] Brian R. Espey,[1,4]
David S. Finley,[3] and Gerard A. Kriss[1,4]
Received 1998 August 17; accepted 1998 December 21

ABSTRACT

We present the final calibration of the Hopkins Ultraviolet Telescope (HUT) for its flight during the Astro-2 space shuttle mission in 1995 March. Aspects of mission operations and instrument performance that affect data quality are described in detail, as are the data reduction procedures applied to the archived data. The sensitivity calibration is defined by a comparison between synthetic spectra and observations obtained in flight of the hot DA white dwarfs HZ 43, GD 71, GD 153, and G191-B2B; the synthetic spectra were calculated by D. Koester using model parameters derived from fits to ground-based spectra. The resulting flux-calibrated spectra for these stars differ from their respective model predictions by less than 3% at all wavelengths, except at the cores of the Lyman lines where the observed line profiles are shallower than the predicted profiles. As an additional consistency check, the HUT spectrum of BD +75°325 was found to differ from the *Hubble Space Telescope* Faint Object Spectrograph spectrum by at most 5% in the region of overlap. The wavelength scale and spectral resolution were calibrated by observations of symbiotic stars and of the coronal star α Aur. The spectral resolution was found to vary from 1.8 to roughly 4.5 Å, depending on wavelength and on the instrument configuration. The internal consistency of the HUT calibration provides a new and important test of white dwarf model atmospheres, as the predicted stellar spectra are more sensitive to changes in model parameters or to shortcomings in the models themselves at wavelengths shortward of 1100 Å than at longer wavelengths. Combining this result with that of the Astro-1 HUT calibration (that a synthetic spectrum of G191-B2B and laboratory flux standards gave results consistent within the laboratory measurement uncertainties) demonstrates that pure hydrogen white dwarfs with effective temperatures of 32,000–61,000 K may be used as primary flux standards down to the Galactic Lyman edge.

Subject headings: space vehicles — stars: fundamental parameters — white dwarfs

1. INTRODUCTION

The second flight of the Hopkins Ultraviolet Telescope (HUT) took place in 1995 March, aboard the space shuttle *Endeavour* as part of the Astro-2 mission (STS 67). This highly successful mission produced 385 observations of 265 celestial objects at far-ultraviolet wavelengths. The full data set has been reduced and calibrated and is being archived at the National Space Science Data Center (NSSDC). The HUT instrument as it flew on the Astro-1 mission was described by Davidsen et al. (1992). Changes to the instrument made for the Astro-2 mission, a brief summary of the mission, and the preliminary instrument calibration are described by Kruk et al. (1995). This paper describes the final calibration in detail. In order to maximize the utility of the archived data to the astronomical community, descriptions are also given of instrument characteristics and aspects of flight operations that affect data quality; the data reduction procedures applied to the archived data are also described.

2. MISSION OVERVIEW

2.1. *Instrument Description*

HUT consists of a 90 cm *f*/2 parabolic primary mirror and a prime focus Rowland circle spectrograph, mounted on an Invar optical bench. A drawing of the instrument may be found in Davidsen et al. (1992). The primary mirror is a weight-relieved Cervit substrate with an Ir coating and an SiC overcoating. The spectrograph consists of a spherical grating with a 400.7 mm radius of curvature, an entrance slit located 0°.5 from the grating normal, and a windowless microchannel plate detector located on the Rowland circle so as to cover the wavelength range 820–1840 Å in first order. The grating consists of a stainless steel substrate with a replicated holographic 600 lines mm^{-1} grating surface and an SiC coating.

The spectrograph entrance apertures are mounted on an eight-position wheel. There are six apertures available for science operations: 12″, 20″, and 32″ diameter circular apertures, a 32″ diameter aperture combined with an aluminum filter, and two long-slit apertures of dimension 10″ × 56″ and 19″ × 197″. The apertures are etched through a mirrored surface that reflects the star field in the vicinity of the target into a slit-jaw camera that is used by the payload specialist for target acquisition and tracking. There is one large (175″ diameter) aperture used only for ground calibrations and a blank position with no aperture that provides a vacuum seal.

The detector consists of two microchannel plates (MCPs) in a chevron configuration. The MCP pores have a diameter of 10 μm, a center-to-center spacing of 12 μm, and a length to diameter ratio of 80:1. The bias angle is 15°, and the pores are oriented so that the angle of the incoming photons relative to the pore axis is never less than 5°. The MCPs are mounted above a phosphor screen anode that is coupled by a fiber optic window to a one-dimensional Reticon photodiode array. The array consists of 1024

[1] Department of Physics and Astronomy, Johns Hopkins University, Baltimore, MD 21218; kruk@pha.jhu.edu, afd@pha.jhu.edu.
[2] Present address: Goddard Space Flight Center, Greenbelt, MD 20771; tbrown@gsfc.nasa.gov.
[3] Eureka Scientific, Inc., 2452 Delmer Street, Suite 100, Oakland, CA 94602; david@eurekasci.com.
[4] Present address: Space Telescope Science Institute, 3700 San Martin Drive, Baltimore, MD 21218; espey@stsci.edu, gak@stsci.edu.

diodes, each 25 μm wide by 2.5 mm tall. An opaque CsI photocathode is deposited directly onto the top surface of the MCPs. A detected UV photon produces roughly 2×10^6 electrons that exit from the MCPs and are accelerated into the phosphor screen. Each electron then produces on the order of 100 visible photons that are transmitted to the photodiodes via the fiber optic window. The MCP-anode gap spacing and voltage are adjusted so that a single event distributes a measurable signal over 10–15 adjacent diodes, which is then centroided with half-diode precision. The signals in the photodiodes are digitized at a rate of 1 MHz, so 1.024 ms are required for a complete scan of the array. The detector design is described in detail by Long et al. (1985), with some minor modifications described by Kruk et al. (1995).

The spectrograph design precludes scrubbing the detector after its final exposure to atmospheric pressure (for a description of scrubbing, see Siegmund 1989). All transfers of the detector from one vacuum system to another (for photocathode deposition or mounting to the spectrograph) were performed in a glove bag purged with dry N_2, but that did not prevent some loss of the effects of the prior scrubbing. As a result, there was some loss of gain in the MCPs during spectrograph alignment caused by exposure to the two strongest argon lines (1048 and 1067 Å) and a concomitant small, but detectable, loss in quantum detection efficiency (QDE) at those wavelengths. The spectrograph was integrated into the telescope approximately 18 months prior to the launch, during which there were numerous functional tests, interface verification tests, and mission simulations. Each test included detector operations, both dark count measurements and calibration lamp measurements. The gain of the detector gradually declined over these 18 months, which we have attributed to slow evolution of adsorbed gas from the walls of the MCP pores. The detector high voltage was adjusted early in the mission to restore the gain to its nominal value. Exposure to bright sources during the mission caused some localized gain reductions that are described below in § 6.

The telescope aperture is covered by two independent semicircular shutter doors. When opened fully, the geometric area of the primary mirror illuminated by each door is 2560 cm^2, for a total of 5120 cm^2. It is also possible to open the doors only part way. During Astro-2 there were two such partial openings that were routinely utilized: one door was closed, and the other opened to expose either 200 or 750 cm^2 of the primary mirror. In addition, one of the two doors has a 50 cm^2 circular aperture that is covered by a sliding plate mechanism. Each door configuration illuminates different portions of the mirror, grating, and detector and illuminates the detector at different angles. Consequently, each such door configuration requires a separate calibration. The most significant effect is the differing illumination of the detector. When both doors are open, the optical beam is $f/2$ in both directions and illuminates the detector equally above and below the dispersion plane. When only one door is fully open, the beam is $f/2$ in the dispersion direction and $f/4$ in the cross-dispersion direction and only illuminates the detector above the dispersion plane. When the one door is open to the 200 or 750 cm^2 position, the illumination is still $f/2$ in the dispersion direction, but only $f/81$ and $f/22$, respectively, in the cross-dispersion direction. The 50 cm^2 opening produces an $f/23$ beam that illuminates roughly the same region of the detector as the 750 cm^2 opening. The various door openings produce somewhat different line-spread functions (LSFs) at the detector surface. The full- and half-aperture door openings have the same relative contributions to the core and tails of the LSF. The 750 and 200 cm^2 openings have the same flux in the tails as the full door opening but relatively less flux in the core, resulting in somewhat poorer spectral resolution. The 50 cm^2 opening produces the narrowest LSF. The LSF is discussed in greater detail in § 15. Ray trace calculations of the illumination of the photocathode by the various door configurations are shown in Figure 1. The differences in regions illuminated can potentially lead to significant differences in the strengths of flat-field features in spectra obtained through different door configurations. The differences in the angles at which the detector is illuminated for the different door configurations can vary slowly with wavelength, leading to concomitant changes in the shape of the effective area curves.

2.2. *Mission Description*

The Astro-2 mission began on 1995 March 2 at UT 06:38:13 with the launch of the space shuttle *Endeavour* (STS 67). The orbit was nearly circular, with an altitude of 346 by 352 km and an inclination of 28°.5. HUT was mounted on a cruciform structure in the payload bay, along with two other UV instruments: the Wisconsin Ultraviolet PhotoPolarimeter Experiment (WUPPE) and the Ultraviolet Imaging Telescope (UIT). The WUPPE instrument is described by Nordsieck et al. (1994); UIT and its on-orbit performance are described by Stecher et al. (1997). The cruciform itself was mounted on the Spacelab Instrument Pointing System (IPS). Instrument activation began at 3^h44^m mission elapsed time (MET). Activation activities included basic instrument functional tests, focusing of the

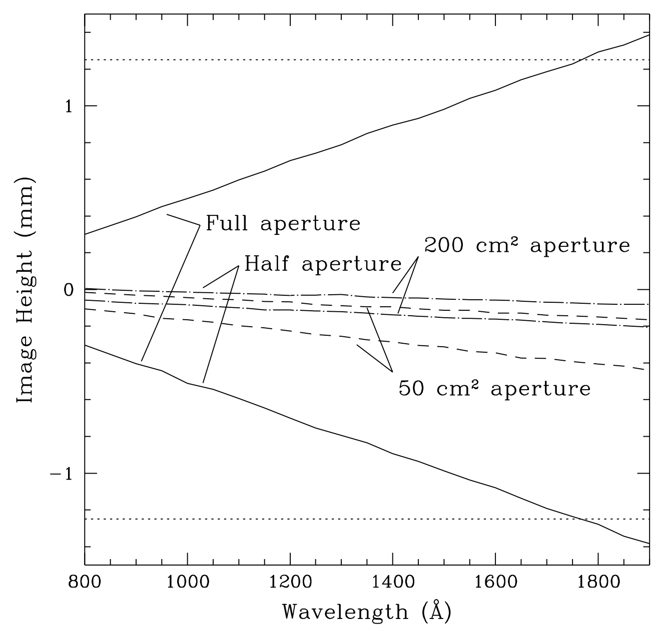

FIG. 1.—Regions of the detector photocathode illuminated by the different aperture door configurations are shown. The dotted lines plotted at ±1.25 mm indicate the boundaries of the detector active area. The solid lines show the positions of the extreme rays produced by the full-aperture door opening, the dashed lines correspond to those from the 50 cm^2 opening, and the dot-dashed lines to those from the 200 cm^2 opening. The half-aperture opening illuminates the lower half of the full-aperture region. The region illuminated by the 750 cm^2 door configuration is not shown explicitly but is essentially the sum of the regions illuminated by the 200 cm^2 door and 50 cm^2 door configurations.

primary mirror/guide star camera system, updates to the relative alignment of each instrument's line of sight with respect to the star trackers, SAA tests (see below), and finally, end-to-end focusing of the primary mirror, spectrograph, and detector. The first science observation for HUT was of P Cygni, beginning at 31^h MET. Science operations continued, with brief interruptions for shuttle water dumps, until the instruments were deactivated at $359^h.6$ MET.

The only focus and alignment adjustments internal to HUT are the three primary mirror actuators. The guide star camera and spectrograph were each internally focused to the spectrograph slit during the telescope alignment preflight. Thus, if the primary mirror were focused on the slit, then the two subsystems should be in focus. During the initial in-flight checkout it was found that the guide star camera focus was indeed best when the primary mirror was at its nominal preflight position. However, some component of the spectrograph had apparently shifted, because the optimal spectrograph focus was obtained when the primary mirror was shifted by about 200 μm from the preflight position. The flat detector surface intersects the curved spectrograph focal surface at two points, which were intended to be at positions corresponding to 1050 and 1350 Å. What was found instead was that the detector intersected the spectrograph focal surface near its ends. At 110^h MET the primary mirror was shifted from its nominal preflight "best-focus" position by 100 μm, which was roughly halfway between the optimal positions for the camera and spectrograph. The mirror was occasionally returned to the best camera focus position for observations that had faint guide stars, crowded fields, or otherwise required good camera performance for a successful target acquisition. The mirror would be moved back to the compromise position following the observation (during the slew to the next target). The spectrograph focus is discussed in detail in § 15.

The detector high voltage was adjusted on several occasions during the mission. There are two different voltages that were adjusted: the MCP voltage, which is the voltage applied directly across the MCPs, and the phosphor voltage, which is the voltage applied to the gap between the back surface of the MCPs and phosphor anode. Shortly after activation (at 31^h MET, during the first observation of P Cygni), the MCP voltage setting was increased from 4 to 5, corresponding to an increase in voltage from 2778 to 2821 V. During the next observation (HD 93521, beginning at 32^h MET), the MCP high voltage was raised first to a setting of 6 (2862 V), and finally to 7 (2904 V). The MCP voltage was not adjusted thereafter during the mission. Pulse height and width distributions were obtained after each adjustment; when these distributions matched those obtained during the preflight instrument calibration the adjustments were stopped.

Detector pulse height and width data were obtained daily throughout the mission, during observations that made use of a variety of aperture door configurations. It was found that the detector gain declined slowly over the subsequent several days, when measured for stars observed through the 50, 200, or 750 cm^2 door configurations (which illuminate a relatively narrow strip of the detector); little or no change was observed when observing through the 2560 or 5120 cm^2 door configurations. The phosphor high-voltage setting was raised one step, from 3 to 4 (from 6845 to 6987 V) to compensate for this decline. The phosphor voltage was first raised prior to the observation of HD 189957 at $139^h.4$ MET as a test, and then finally at $159^h.2$ MET during the second observation of P Cygni. The phosphor voltage was not adjusted thereafter. This increase in phosphor voltage resulted in an apparent increase in count rate of 4.4%, independent of wavelength. The pulse height distributions declined slightly over the following day or so and remained stable thereafter. Our best estimate is that the instrument sensitivity for observations obtained through the 50, 200, and 750 cm^2 door configurations declined gradually over the 3 days prior to 159^h MET by 4.4%. Because the effect was small, and the time-dependence was not well established, no correction for this decline was applied to the archived data. Further information on detector gain and its consequences is given in §§ 5 and 6.

2.3. *Observation Description*

A typical HUT observation sequence began with the slew from the previous target, during which time one of the ion pumps was running. Pumping was required for a few minutes out of every few hours to maintain the pressure within the spectrograph at levels compatible with operation of the windowless detector. During slews the spectrograph was sealed; during observations the only vent path for the spectrograph was through the selected entrance slit, none of which was large enough to prevent pressure buildup. Following completion of the slew, the pump was turned off, the detector high voltage was turned on, and the aperture doors, spectrograph slits, and guide star camera were commanded to the configuration desired for the upcoming observation. At the same time, the IPS and ASTROS Star Tracker (AST) were performing a field identification and a coarse attitude adjustment. Once stars were identified in the HUT slit-jaw camera, a fine attitude adjustment was made to center the target in the HUT slit. At this point the payload specialist performed a series of steps to co-align WUPPE to HUT and then issued a BEGIN command. The BEGIN command starts the exposure sequences for HUT, WUPPE, and UIT and causes the Image Motion Compensation System (IMCS) to begin sending pointing error data from its gyroscopes to WUPPE and UIT.

During an observation, the IPS maintained the line of sight (LOS) as it was at the time of the BEGIN. The pointing stability for the Astro-2 mission was usually excellent: in most cases the jitter was $\lesssim 1''$ rms, and it rarely exceeded $2''$. The delay between the centering of the target in the HUT slit and the BEGIN was typically 1–2 minutes, during which there might have been several arcseconds of drift. In some cases, the result was that the target was near the edge of the HUT slit, so that the small amount of jitter could cause significant loss of flux. There were also occasions where thermally induced shifts in co-alignment of HUT with respect to the star trackers could cause offsets of several arcseconds during an observation. Such drifts were corrected manually by the payload specialist. During some observations the instrument configuration would be changed at preplanned times for certain purposes: the primary mirror would be tilted to observe at an offset position, a different slit might be selected (for example, to use a larger slit for a diffuse source after crossing the terminator into night), changing the aperture door opening, or stopping accumulation of the spectrum for a few minutes to obtain detector diagnostic data. Finally, the observation would be terminated at a predetermined time (typically when the earth limb angle fell below 15°). In many cases we were able to track the target down to an earth limb angle of 10°; however, we found that absorption by atmospheric N_2 could significantly affect the spectra of objects shortward of about 950 Å at limb angles $\lesssim 12°$. For all archived spectra we therefore discarded data obtained at limb angles less than 15°.

If the observing sequence was set up to have the planned observation slit in position for the acquisition, then an airglow spectrum would be obtained for several minutes before the target entered the slit. If the target was bright enough to see in the slit-jaw camera, however, we frequently performed the acquisition with the blank slit in place. In this case the spectrum obtained prior to the BEGIN command was detector dark current only.

The HUT instrument produced a complete cumulative spectral histogram every 2 s, commencing with instrument setup for an observation. Therefore, the exposure effectively began whenever the object entered the HUT slit, regardless of when the BEGIN command was issued. There was also a complete set of instrument engineering data produced every 2 s, which was downlinked along with the histogram. The AST star centroid data were downlinked every second, beginning within 20 s of a command to the AST to acquire guide stars. This command was ordinarily sent shortly after completion of the slew but would occasionally be repeated later in the acquisition or during the observation itself. The AST data were used by our data reduction software for computing corrections for pointing jitter, so such resets reduced the portion of the exposure that could be corrected for these effects. The IMCS gyro pointing errors were sampled and downlinked at a rate of 50 Hz, starting on issuance of the BEGIN command by the payload specialist.

Integration times could be determined by two independent methods. Absolute times (Greenwich mean time) were provided by the Spacelab Experiment Computer (EC) with an absolute accuracy of ± 10 ms and a relative accuracy of 3 ms over a 7 day period. The HUT Dedicated Experiment Processor (DEP) and Spectrometer Processor (SP) were synchronized to the EC via a 4 Hz clock pulse. Each data message sent by the SP includes the GMT at the beginning of the 2 s spectral integration contained in the message. In addition, each data message contains the number of Reticon scans accumulated since the last data message and the total number of scans since the SP spectral histogram was cleared. Because each scan requires 1.024 ms to complete, counting the scans from the beginning to end of an exposure provides the effective integration time for the data that were actually collected. Differences between the exposure times computed from the scan counts and from the EC GMT are generally much less than 1 s.

2.4. *Airglow*

Airglow lines generally vary independently of one another during an observation and from one LOS to another. However, if an airglow measurement were obtained at a representative earth limb angle and the observation did not span a terminator crossing, the airglow spectrum obtained during an acquisition could provide a reasonable template for an airglow subtraction. Typical airglow spectra from the day and night sides of the orbit are shown in Figures 2*a* and 2*b*, respectively. On the night side of the orbit the only lines ordinarily seen are from H I, although occasionally weak O I emission is seen at 1304 and 1356 Å. On the day side of the orbit the O II 834 Å airglow line serves as a rough reference for the strength of the other airglow lines that may be contaminating an observation, because it is well below the Galactic Lyman edge and is therefore not mixed with flux from astronomical sources beyond the solar system. The use of SiC coatings on the optics for Astro-2 resulted in a significantly lower effective area at EUV wavelengths relative to Astro-1; hence, the He I 537, 584 Å, and O I 539 Å airglow lines that appeared in second and third orders in Astro-1 spectra are generally not detectable in Astro-2 spectra.

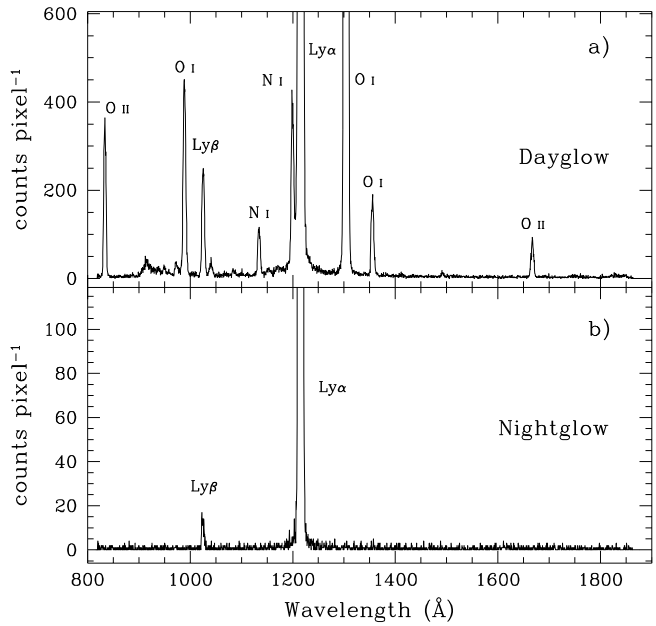

FIG. 2.—Panel *a* shows a typical airglow spectrum obtained on the day side of the orbit; panel *b* shows a typical airglow spectrum obtained on the night side. Both spectra were obtained through the 20″ aperture. The durations of the exposures were 1490 s for the day and 1300 s for the night. The most prominent emissions have been labeled; the O II emission at an apparent wavelength of 1668 Å is the 834 Å line appearing in second order. The peak intensities of the off-scale lines are 25,500 counts pixel^{-1} for the day side Lyα, 6900 counts pixel^{-1} for the OI 1304 Å, and 1700 counts pixel^{-1} for the night side Lyα.

Grating-scattered Lyα airglow emission is comparable to the detector dark rate on the night side of the orbit; on the day side it is the dominant source of background.

2.5. *South Atlantic Anomaly*

The time of launch was selected to minimize the time spent traversing the South Atlantic Anomaly (SAA) on the night side of the orbit. During instrument activation two tests were performed to determine the effect of the SAA on HUT. The first test measured changes in the dark current in the guide star camera; no effects were seen. The second test measured changes in the detector dark current, which was found to increase from less than 1 counts s^{-1} to about 30 counts s^{-1} at the center of the SAA. HUT observations were subsequently performed through SAA passes, although only relatively bright objects were scheduled at such times.

2.6. *Calibration Approach*

The sensitivity calibration of HUT is defined by models of hot DA white dwarfs. The model parameters are determined from fits to the Balmer line profiles of the stars performed by Finley, Koester, & Basri (1997; FKB hereafter) and normalized to the *V* magnitude. Three DA's were used to define the sensitivity for full-aperture observations: HZ 43, GD 71, and GD 153. These stars, along with G191-B2B, have been used to define the calibration of the *Hubble Space Telescope* (*HST*) Faint Object Spectrograph (FOS) (Bohlin 1996) and are being used for the Space Telescope Imaging Spectrograph (STIS) (R. C. Bohlin 1997, private communication; Kimble et al. 1998). FOS calibrations derived from each of these stars independently were consistent with one another to $\lesssim 2\%$ over the wavelength range 1150–8000 Å (Bohlin, Colina, & Finley 1995). These stars range in effective temperature from 32,300 to 50,000 K and therefore have very different Lyman line profiles. This aids in removing any resolution-dependent effects from the final sensitivity curve. These stars are also known to have pure hydrogen photospheres, with no trace of heavy elements (Dupuis et al. 1995). Finally, these stars all had good visibility on the night side of the orbit for our mission, so that complications from airglow contamination were minimized. A model of the star G191-B2B was used to define the calibration of the *International Ultraviolet Explorer* (*IUE*) final archive (Nichols & Linsky 1996). The model is similar to the ones being used by us and *HST*, but it is normalized somewhat differently (see Kruk et al. 1997 and references therein).

The sensitivity calibration for the reduced aperture door configurations is determined by observing suitable stars through multiple door configurations and fitting a low-order polynomial to the ratio of the observed fluxes (the sensitivity for the 750 cm^2 door configuration was also calibrated directly by a model of G191-B2B). This polynomial is then multiplied by the sensitivity curve for the larger door opening to obtain the sensitivity curve for the smaller opening. This technique preserves any door-dependent large-scale differences in the wavelength dependence of the sensitivity but avoids introducing any structure on small or intermediate scales. The motivation for this approach is that the wavelength dependence of the instrument sensitivity is dominated by that of the SiC reflectivity, the grating groove efficiency, and the photocathode quantum efficiency. The first two contributions will be independent of the door configuration, but the third depends on the angles of the incoming photons and therefore may differ from one door configuration to the next on large wavelength scales.

The stability of the sensitivity calibration was monitored primarily by obtaining multiple observations of the white dwarf GD 394. This star was chosen because it was bright enough to obtain a good spectrum in less than 1000 s and because it had good visibility on the day side of the orbit (this monitoring function was relatively insensitive to the presence of airglow, and, given the relatively short duration of the mission, the night portions of the orbits were oversubscribed with faint targets that were essentially unobservable during the day). The two observations of RE 1738+669 were also utilized for this purpose.

Calibration of the wavelength scale and spectral resolution was done by observations of the coronal star α Aur and the symbiotic stars AX Per, V1016 Cyg, RR Tel, EG And, Z And, and AG Dra, which have strong emission lines that are much narrower than the HUT spectral resolution.

3. OBSERVATIONS AND DATA REDUCTION

Basic information on each observation used for sensitivity and flat-field calibrations is given in Table 1, and information on each observation used for wavelength and spectral resolution calibrations is given in Table 2. Each spectrum is listed separately: if the aperture door configuration or spectrograph slit was changed during a single pointing to obtain a relative calibration or check on photometry, there are multiple entries for that pointing in the table. Additional information for each observation is given below following the description of the basic data reduction procedure. Unless otherwise noted, the count rate fluctuations during each observation were consistent with Poisson statistics. The last column in Tables 1 and 2 is the offset of the primary mirror from the preflight nominal focus position.

3.1. *General Data Reduction Procedures*

The entire set of spectra used for sensitivity and flat-field calibrations was reduced 3 times. The first reduction included no corrections for flat-field features or for changes in sensitivity during the mission and used the preliminary sensitivity calibration described by Kruk et al. (1995). The resulting spectra were then used to determine the flat-field and sensitivity time-dependence corrections, in the manner described in the corresponding sections below. The data were then rereduced, including these corrections but still with the preliminary sensitivity calibration. The full-aperture sensitivity was then derived from a comparison of the fully corrected count rate spectra produced by the next to last step in the data reduction procedure given below with the corresponding synthetic spectra for HZ 43, GD 71, and GD 153. The sensitivity for other aperture door configurations was then determined in a similar manner by observations of HZ 43, GD 153, and G191-B2B and by ratios of spectra of a given star obtained through multiple door configurations. The sensitivity calibrations are described in detail in subsequent sections. Finally, all the spectra were reduced a third time with the final calibrations.

There were five significant differences between this data reduction procedure and that used to perform the preliminary calibration reported by Kruk et al. (1995): (1) photometric corrections were computed from the pointing errors; (2) more accurate dead-time corrections were computed; (3) better corrections for flat-field features and changes in sensitivity as a function of time were available; (4) the spectra were corrected for EUV flux present in second and third order; (5) the spectral resolution was improved by corrections for pointing jitter.

The resulting changes to the spectra were typically on the order of a few percent, but the internal consistency of the calibration that resulted was noticeably better than that of the (already good) preliminary calibration.

The data reduction procedures used for the white dwarf observations were somewhat more involved than for most HUT observations because of the possible contamination of the first-order spectrum by EUV flux that would be detected in second and third orders. The steps in this procedure are listed below; those that involve specific calibrations are discussed in detail in subsequent sections of this paper, and the remainder are described following the list of steps.

1. Accumulate spectrum between designated start and stop times, with and without correcting for pointing jitter. Compute a photometric correction by fitting the slit throughput function to pointing errors and observed count rates.

TABLE 1

ASTRO-2 HUT PHOTOMETRIC CALIBRATION OBSERVATIONS

Star	Start Time UT	Start Time MET (hour)	Exposure (s)	Door (cm^2)	Slit Diameter (arcsec)	Photometric Correction	Day or Night (%)	Airglow Subtracted?	Jitter Corrected?	Mirror Δ (μm)
HZ 43	Mar 3 17:51:15	35.2	420	5120	20	1.3598	100 N	Yes	Yes	0
HZ 43	Mar 3 18:00:15	35.4	258	2560	20	1.264	100 D	No	Yes	0
HZ 43	Mar 4 22:52:39	64.2	552	5120	20	1.2306	100 N	No	Yes	0
HZ 43	Mar 15 23:49:07	329.2	696	5120	20	1.004	100 N	No	No	−100
HZ 43	Mar 16 00:02:03	329.4	482	5120	30	1.001	100 N	No	No	−100
GD 71	Mar 6 23:15:52	112.6	1178	5120	20	1.0128	100 N	No	No	−100
GD 153	Mar 7 23:54:06	137.3	478	5120	20	1.0167	100 N	No	No	−100
GD 153	Mar 8 00:03:32	137.4	1044	2560	30	1.0015	100 N	No	No	−100
G191-B2B	Mar 7 00:33:14	113.9	508	200	20	1.0262	100 D	No	No	−100
G191-B2B	Mar 7 00:42:56	114.1	1214	750	20	1.0186	89 N	No	No	−100
GD 394	Mar 4 23:31:17	64.9	94	5120	20	1.900	100 D	Yes	No	0
GD 394	Mar 6 02:47:20	92.1	480	5120	20	1.0030	100 D	Yes	No	0
GD 394	Mar 6 02:56:42	92.3	360	5120	30	1.000	100 D	Yes	No	0
GD 394	Mar 6 03:04:02	92.4	28	750	30	1.000	100 D	Yes	No	0
GD 394	Mar 8 00:47:42	138.2	302	5120	20	1.0230	100 D	Yes	No	−100
GD 394	Mar 8 00:54:04	138.3	82	750	20	1.0190	100 D	Yes	No	−100
GD 394	Mar 11 01:44:44	211.1	582	5120	20	1.2500	100 D	Yes	No	−100
GD 394	Mar 11 01:55:44	211.3	440	5120	30	1.0050	100 D	Yes	No	−100
GD 394	Mar 16 11:24:42	340.8	550	5120	30	1.0008	100 D	Yes	No	−100
GD 394	Mar 16 11:35:10	340.9	354	750	30	1.0025	100 D	Yes	No	−100
RE 1738+669	Mar 10 02:02:18	187.4	944	5120	20	3.6780	100 N	No	Yes	−100
RE 1738+669	Mar 10 02:18:44	187.7	874	5120	20	1.0804	100 N	No	No	−100
RE 1738+669	Mar 16 17:52:54	347.2	724	5120	20	1.0998	100 D	Yes	No	−100
RE 1738+669	Mar 16 18:06:20	347.5	226	5120	30	1.0009	100 N	No	No	−100
NGC 1360	Mar 15 03:27:07	308.8	396	750	30	1.0009	100 D	Yes	No	−100
NGC 1360	Mar 15 03:34:49	308.9	530	750	30	1.0007	100 D	Yes	No	−100
BD +75°325	Mar 8 16:30:26	153.9	666	200	20	1.0043	100 N	No	No	−150
BD +75°325	Mar 8 16:45:32	154.1	560	50	20	1.0062	100 N	No	No	−150
LS V 46°21	Mar 15 14:29:15	319.9	270	5120	20	1.0050	100 D	No	No	−100
LS V 46°21	Mar 15 14:35:01	319.9	486	750	20	1.0011	73 N	No	No	−100

TABLE 2

ASTRO-2 HUT WAVELENGTH CALIBRATION OBSERVATIONS

STAR	START TIME UT	START TIME MET (hour)	EXPOSURE (s)	DOOR (cm^2)	SLIT DIAMETER (arcsec)	PHOTOMETRIC CORRECTION	DAY OR NIGHT (%)	AIRGLOW SUBTRACTED?	JITTER CORRECTED?	MIRROR Δ (μm)
α Aur	Mar 3 03:41:45	21.1	716	5120	20	23.048	100 N	No	No	−150
α Aur	Mar 3 04:00:11	21.4	286	5120	20	1.0047	100 N	No	No	−50
α Aur	Mar 3 04:07:11	21.5	314	5120	20	1.0362	100 N	No	No	0
α Aur	Mar 3 05:13:23	22.6	288	5120	20	1.5480	100 N	No	No	+100
α Aur	Mar 3 05:20:23	22.7	310	5120	20	1.6306	100 N	No	No	+150
α Aur	Mar 3 05:28:53	22.8	310	5120	20	1.4050	100 N	No	No	+200
α Aur	Mar 3 05:36:17	23.0	328	5120	20	1.5764	100 N	No	No	+250
AG Dra	Mar 16 19:14:24	348.6	632	2560	12	1.0641	100 D	No	Yes	−100
AX Per	Mar 4 02:15:59	43.6	548	5120	20	1.5631	100 D	No	Yes	0
AX Per	Mar 4 02:27:33	43.8	306	5120	20	1.0118	100 D	No	Yes	+50
CH Cyg	Mar 13 02:40:01	260.0	988	5120	20	1.0795	100 D	No	Yes	−100
EG And	Mar 3 17:02:07	34.4	708	5120	20	1.4548	100 D	No	Yes	0
EG And	Mar 3 17:16:31	34.6	356	5120	20	1.2281	100 D	No	Yes	−50
EG And	Mar 15 06:31:33	311.9	920	5120	20	1.0343	100 D	No	Yes	−100
RR Tel	Mar 12 14:21:53	247.7	1080	750	20	1.0167	100 D	No	No	−100
V 1016 Cyg	Mar 6 23:59:08	113.3	614	2560	12	1.6483	100 D	No	Yes	−100
Z And	Mar 6 01:21:46	90.7	1368	5120	20	1.0091	100 D	No	Yes	0

2. Correct for detector dead time; see § 5.3.
3. Correct for phosphor persistence effects; see § 5.4.
4. Subtract dark count; see § 5.1.
5. Apply flat-field correction, if not already done in step 1; see § 6.
6. Subtract a template airglow spectrum if there is one available.
7. Multiply by the photometric correction calculated in step 1.
8. Subtract EUV flux (flux shortward of 911 Å) in first, second, and third orders. Save first-order values to add back later. All that should remain below 912 Å is scattered light. The EUV flux is computed from the stellar model atmosphere, opacity of the interstellar medium, opacity of the Earth's upper atmosphere as a function of limb angle during the observation, and the preflight calibration of the instrument higher order sensitivity (see § 10). The maximum correction found for EUV flux was for HZ 43, where it was roughly 1.4% of the first-order flux at 1550 Å.
9. Subtract scattered light: compute the mean counts pixel^{-1} in the range 840–885 Å, and subtract from each pixel in the spectrum. This wavelength range is free from airglow. This procedure also corrects for any detector dark current not accounted for in step 4.
10. Add back first-order EUV counts (815–911 Å) subtracted in step 8. This is the theoretical estimate of the flux at these wavelengths and is included only to alert the user that a real signal may be present.
11. Subtract second-order FUV (>912 Å) counts. The first-order counts in the range 905–932 Å are scaled by the ratio of second–to–first-order spectrograph efficiency (determined from the preflight laboratory calibration), distributed into the corresponding second order wavelength bins, and subtracted pixel by pixel from the first-order spectrum (at wavelengths from 1810 to 1864 Å, respectively).
12. Divide by exposure time.
13. Multiply by the inverse sensitivity curve to obtain the fluxed spectrum. The inverse sensitivity for each door state is described in §§ 8 and 9, and the correction for variations in sensitivity during the mission is described in § 4.

Stars other than the white dwarfs were reduced using the same procedures as for the archived data as described in § 16 below. For many of the symbiotic stars the archived spectra were used for the resolution function analysis, without any rereduction to minimize the airglow. As a consequence, many of these spectra have relatively large photometric corrections because the exposure time includes the target acquisition period.

Each spectrum was reduced with and without corrections for pointing jitter. Jitter correction is performed by shifting the spectrum obtained in each 2 s integration to correct for displacements of the point-source image at the spectrograph slit relative to the center of the slit. Flat-field corrections are applied to each 2 s integration prior to shifting the spectrum. The telemetry required for performing jitter corrections was usually not present for the entire observation; hence, unless the spectral resolution was detectably worse for the uncorrected spectrum (typically when the rms jitter was greater than 1"5 in the dispersion direction), then the uncorrected spectrum was used, as it had a longer effective integration time. The cases where the jitter-corrected spectrum was used are noted in Tables 1 and 2.

The HUT slits are large relative to the telescope point-spread function; therefore, if the target is well centered in the slit the data reduction software cannot use the correlation of count rate and pointing errors to determine the position of the star within the slit and hence the absolute wavelength scale. We therefore found it necessary in several instances to shift the spectra manually by a few pixels until the observed photospheric absorption lines matched the wavelengths of the lines in the model spectra (see below). All shifts of the spectra, including those performed for the jitter corrections, are only by integer pixels to avoid smoothing the data.

The photometric correction factor for each spectrum is also given in Tables 1 and 2. This correction is determined by fitting the observed count rate as a function of time during the observation with a rate predicted from the pointing errors (the free parameters in the fit are the "true" count rate and an arbitrary initial offset of the image point-spread function with respect to the slit). The correction factor is the ratio of the fitted "true" count rate to the observed mean rate. This correction is described in greater detail in Appendix A of Kruk et al. (1997).

The scattered light correction is a constant value that is subtracted from all pixels. The scattering profile for the HUT grating, given in Kruk et al. (1995), consists of a narrow peak with long tails, so the subtraction of a constant scattered light background is adequate in most circumstances. Exceptions would include analyses requiring detailed fits to the shape of strong emission or absorption lines or fits to weak features on the sides of such lines. In such cases the user will want to convolve a model spectrum with the scattering profile given by Kruk et al. (1995).

3.2. *Individual Observations*

3.2.1. *Photometric Calibration Observations*

HZ 43.—There were three observations of HZ 43. The first observation was split between full- and half-aperture door openings to provide calibrations of both configurations. The full-aperture exposure was obtained during orbital night; the half-aperture exposure was obtained during orbital day. The pointing stability for this early observation was quite poor. The star was fully in the slit for only about 100 s of each exposure, but that was sufficient to determine the true incident flux level. Intervals where the count rate was less than 50% of the peak were discarded. Intervals where the star was fully out of the slit were used to measure the airglow spectrum. Only the first few minutes of the half-aperture data were used; because these data were obtained immediately following the terminator crossing, the airglow spectrum is still dominated by Lyα, with little or no apparent emission from O I or N I.

The pointing stability for the second HZ 43 observation was much better than for the first observation but was just large enough in the dispersion direction (2"3 rms) to benefit from jitter correction of the spectrum. The pointing accuracy was also poor: the star passed through the center of the slit during the target acquisition but then settled near the edge of the slit. The photometric correction program calculated a correction factor of 1.23. A decline in detector response at 1304 Å is just barely discernible.

The third HZ 43 observation was obtained very late in the mission. The star was well centered in the slit and the pointing jitter was $\lesssim 1''$ rms. The 20" diameter aperture was used for the first 696 s of the observation, after which the

30″ diameter aperture was used to verify that we were indeed capturing the full flux from the star. The source count rate was the same for both apertures, and the count rate fluctuations were consistent with Poisson statistics in both slits. The decline in detector response at 1304 Å is now quite substantial, and the response at Lyα is almost nil.

GD 153.—There was one observation of GD 153, but the exposure was split between full- and half-aperture door openings to provide a calibration of the half-aperture instrument sensitivity. The rms pointing jitter was $\lesssim 1''$ in both axes throughout the observation. The final 4 minutes of the observation were in daylight and were discarded for calibration purposes.

GD 71.—There was one observation, entirely in orbital night. The pointing was quite stable, with rms jitter $\lesssim 1''$. The fluctuations in count rate were consistent with Poisson statistics, apart from one $\sim 4''$ excursion lasting about 6 s during which the count rate dropped by about 20%. The overall photometric correction was just over 1%. The decline in detector response at 1304 Å is now clearly visible.

G191-B2B.—There was one observation, split between the 750 and 200 cm^2 door openings. The 200 cm^2 door observation was during the day, but airglow other than Lyα was insignificant (the Lyα emission was sufficient to fill in the photospheric absorption profile). The first ~ 140 s of the 750 cm^2 data were obtained during the day, the remainder at night. In neither spectrum is there any evidence for the O II 834 Å line, indicating that the reduced door aperture resulted in negligible airglow outside of Lyα.

GD 394.—There were five observations of GD 394. All observations were on the day side of the orbit. The first observation produced only 94 s of data with the star in the slit, but the airglow spectrum obtained during the remainder of the observation served as a template for correcting the other four observations. The observation at 92^h MET was split into three parts: full aperture with 20″ slit, full aperture with 30″ slit, and 750 cm^2 aperture with 30″ slit. The source count rate did not change when the larger slit was put in place, and fluctuations in the count rate were consistent with Poisson statistics, indicating that both spectra were photometric. The third segment was intended to provide a measurement of the sensitivity of the instrument throughput at 750 cm^2 aperture relative to the full aperture but was too brief to be useful. The observation at 138^h MET was split into two segments: one at full aperture and one at the 750 cm^2 aperture. In this case also the 750 cm^2 exposure was too brief to be useful. The observation at 211^h MET began with the 20″ diameter slit, but the count rate fluctuations made it apparent that the star was located near the edge of the slit. The 30″ diameter slit was put in place, after which the count rate fluctuations were consistent with Poisson statistics. The spectrum obtained through the 20″ slit was normalized to match the second spectrum. The observation at 340^h MET was split into two parts: the first provided a 10 minute exposure with the doors opened to full aperture, and the second provided a 6 minute exposure with the doors set to the 750 cm^2 opening. The rms pointing jitter was less than 1″ throughout, although there was a single 4″ offset in the dispersion direction roughly midway through the 750 cm^2 exposure. The 30″ spectrograph aperture was used for both exposures and the photometric corrections were negligible.

BD +75°325.—This star was observed through the 200 and 50 cm^2 door openings. The spectral type of this star is sdO, not DA, but it is one of the *HST* and *IUE* standard stars and was convenient for the purpose of obtaining a relative calibration of the instrument sensitivity through these two door openings. The observation was entirely in orbital night, and the small door openings employed further reduced the airglow. The pointing stability was quite good, with an rms jitter of only 0″.8 in the dispersion direction and 1″.0 in the transverse direction.

NGC 1360.—The central star of this planetary nebula has a spectral type of sdO, not DA, but it was chosen because it is bright enough to obtain a good spectrum through the 750 cm^2 door in less than a kilosecond and its spectrum contains few features. The star was observed through the 30″ diameter spectrograph slit; the HUT primary mirror was used to shift the star by 4″.3 along the dispersion direction at the beginning of the observation and then by 8″.6 in the opposite direction halfway through the observation. This shifted the second spectrum by six detector pixels with respect to the first spectrum, separating stellar spectral features from potential "flat-field" features intrinsic to the detector. This observation took place very late in the mission, so any features induced by exposure to bright objects will be present. The 750 cm^2 door opening illuminates the same region of the detector as the 200 and 50 cm^2 openings. This region of the detector sustained the highest event rates per unit area over the course of the mission. Five minutes of airglow were obtained during the target acquisition, which was relatively weak because of the small door opening. Also present was emission from the planetary nebula: He II λλ1085, 1640, C IV λ1550, and possibly some very weak O VI. The airglow and nebular emissions were scaled by exposure time and subtracted from the stellar spectra. The pointing jitter was about 1″.0 for both axes throughout the observation, with no evidence for long-term drifts. No corrections for pointing jitter were applied for the flat-field analysis (including such corrections had no discernible effect).

LS V 46°21.—This DAO star is the central star of the planetary nebula Sh 2−216. This star was observed through both the 5120 and 750 cm^2 door openings in order to obtain a relative calibration. The full-aperture observation was entirely on the day side of the orbit; however, there is almost no sign of airglow emission (perhaps because the LOS was close to the local zenith).

RE 1738+669.—This star was not intended to be used for calibration but was observed to test DA models at high temperatures. It was observed twice during the mission, however, permitting it to serve as a test of the correction for changing instrument sensitivity as a function of time. The first observation had stable pointing (rms jitter less than 1″), but with poor accuracy. For most of the first 1000 s, the star image was mostly out of the slit (with count rates of 15%–50% of the peak). The payload specialist then adjusted the pointing by about 10″, causing the count rate to jump strongly and then remain constant for the next 400 s. The count rate then fell slowly to about 85% of the peak over the final 300 s. Table 1 shows these two portions of the observation separately. Dead-time corrections were applied separately to the two portions of the observation. The photometric correction program was able to do a very good job of matching the count rates computed from the pointing errors to the observed count rates for the entire observation: after this correction, the normalization of the spectrum was found to be only 3% low relative to the second observation. The second pointing began about 12 hours prior to the end of science operations for the mission. The observation began on the day side of the orbit, and 200 s of airglow data were obtained during target acquisition. The pointing was stable (rms jitter was 1″–1″.4), but the count rate fluctuations were about 40% greater than expected from Poisson statistics. The 30″ diameter slit was therefore put in place following the terminator crossing into night, after which the count rate fluctuations fell to the expected level. The airglow spectrum obtained during acquisition was used to correct the day spectrum, but no airglow subtraction was performed on the night side data.

Wolf 1346.—Spectra of this cool DA white dwarf were used for characterizing flat-field features. Descriptions of these observations and the corresponding data reduction have been given by Koester et al. (1996) and will not be repeated here. The final reduced spectra for each of the photometric calibration observations are shown in Figure 3.

3.2.2. *Wavelength and Spectral Resolution Calibration Observations*

α Aur.—This star was observed at the end of the instrument activation period at the beginning of the mission. During this observation, the primary mirror focus position was stepped from −200 to +250 μm relative to the preflight best-focus position, in order to determine the best in-flight focus. There were some problems with target acquisition this early in the mission, so no data were obtained at the −200 or −100 μm positions, and little was obtained at −150 μm. In addition, it appears that there were significant pointing excursions during all of the exposures. Unfortunately, the IMCS had not been fully activated at the time of this observation, so it was not possible to correct the data for jitter. The photometric correction factors were computed from an analysis of the count rate statistics during each exposure, and the results are generally consistent to better than 10%. This observation occurred before the detector high voltage was raised from its preflight settings, so it is possible that there is an additional systematic uncertainty in the absolute flux levels. Our continuum fluxes for this star are in fact about 25% lower than those reported by Linsky et al. (1995).

AG Dra.—This star was observed very late in the mission, at the then default primary mirror focus offset of −100 μm. Approximately 15 minutes into the observation the 20″ diameter slit was switched to the 12″ diameter slit. Since the star was bright enough to require the use of the half-aperture door configuration, the airglow was essentially negligible apart from O I 1304 Å with the smaller slit in place. Only the data obtained through the 12″ slit were used in this work. The pointing was quite stable in this period, with an rms jitter of about 0″.7 and a gradual drift of 1″-2″. The star was apparently near the edge of the smaller slit, however, because even this small jitter gave rise to measurable fluctuations in count rate. The photometric correction program tracked the changes in count rate very well, so the jitter correction is expected to be accurate.

AX Per.—This star was observed shortly after the start of science operations in the mission. The observation was split

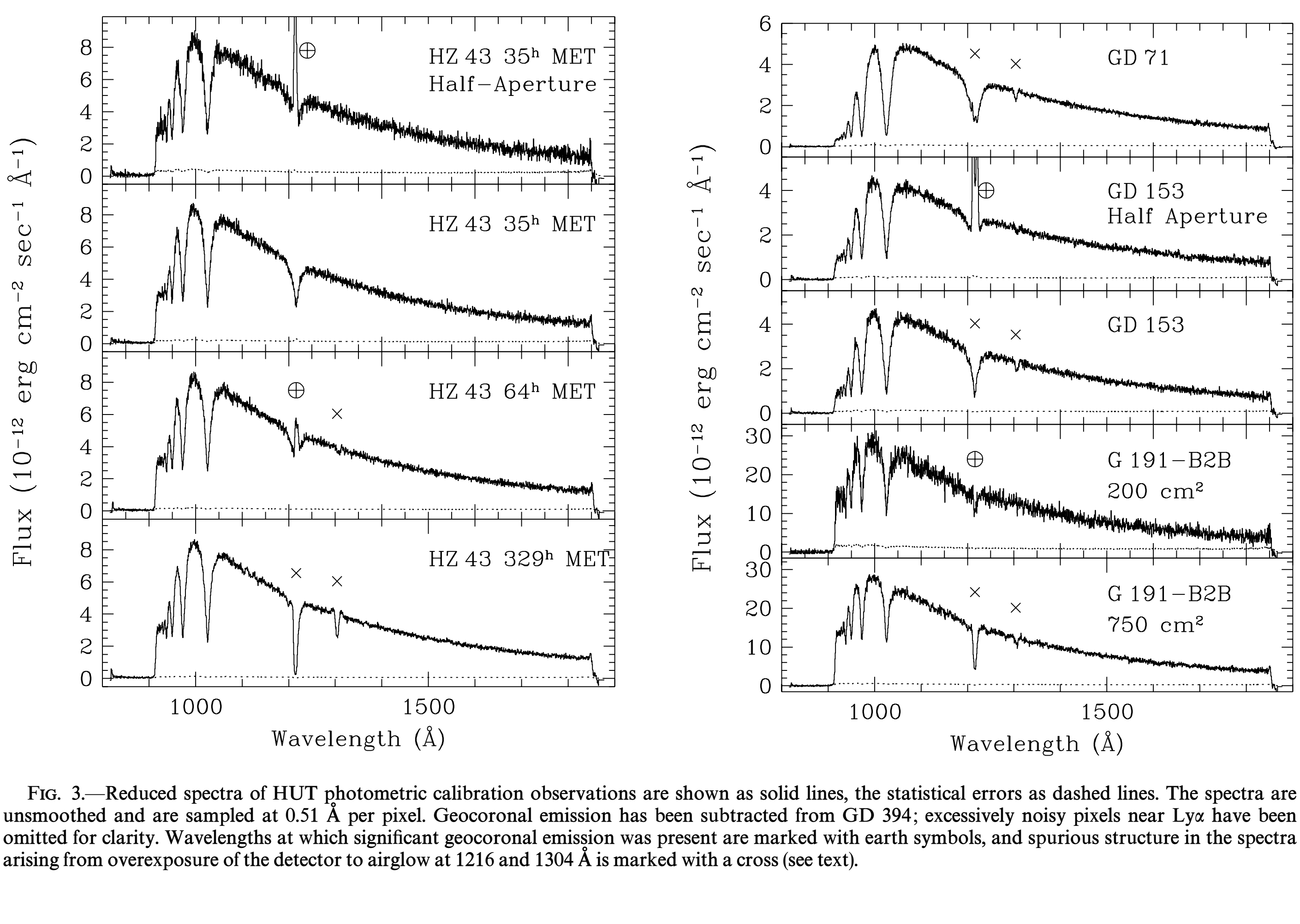

FIG. 3.—Reduced spectra of HUT photometric calibration observations are shown as solid lines, the statistical errors as dashed lines. The spectra are unsmoothed and are sampled at 0.51 Å per pixel. Geocoronal emission has been subtracted from GD 394; excessively noisy pixels near Lyα have been omitted for clarity. Wavelengths at which significant geocoronal emission was present are marked with earth symbols, and spurious structure in the spectra arising from overexposure of the detector to airglow at 1216 and 1304 Å is marked with a cross (see text).

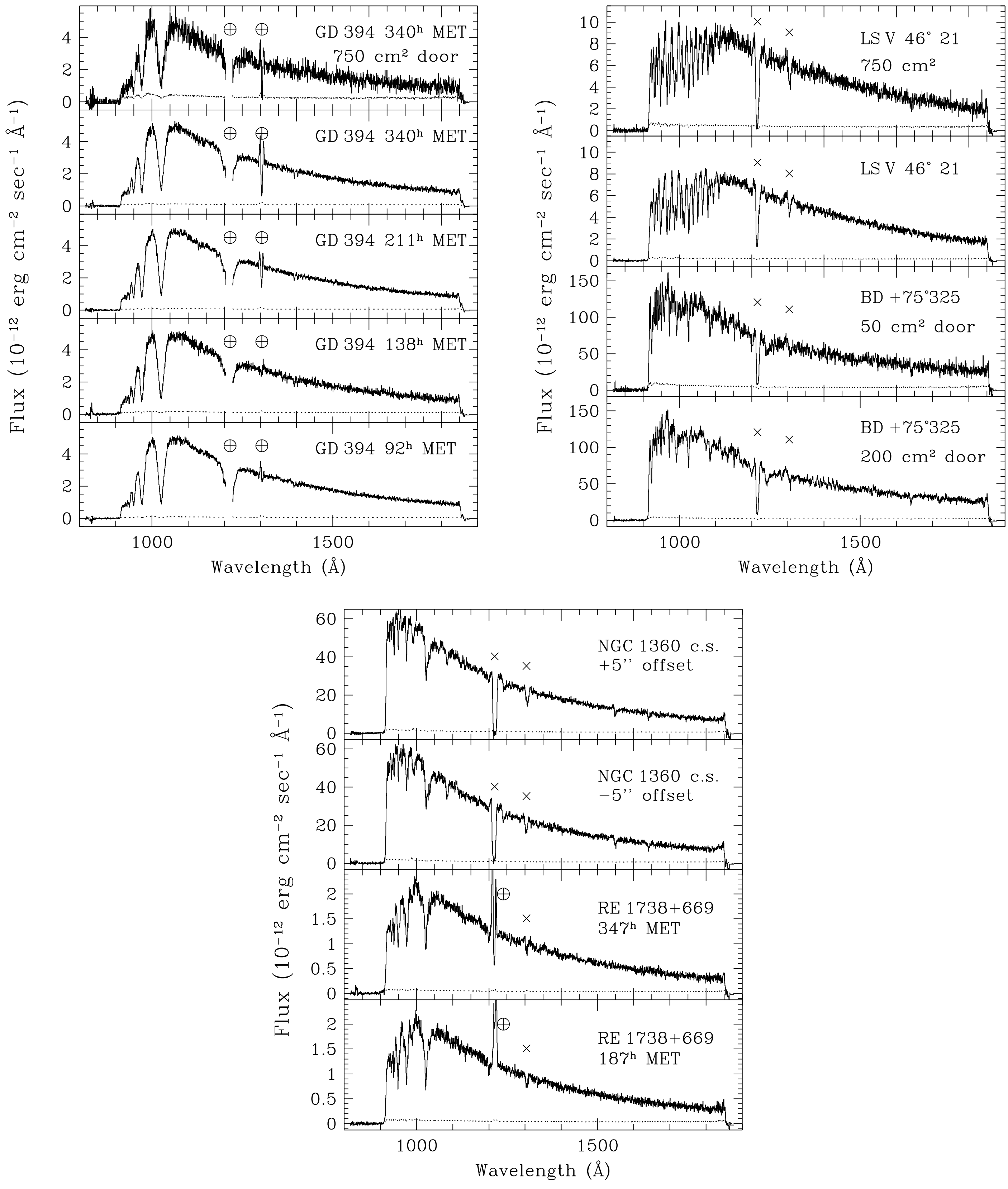

FIG. 3.—*Continued*

between three primary mirror focus offsets to supplement the α Aur data obtained during activation. The third exposure was too brief to provide adequate signal-to-noise ratios (S/Ns) for the resolution analysis and was not used. The pointing was stable for the two exposures that were used; the large photometric correction factor for the first exposure results from the fact that the archived spectrum contains some of the target acquisition period. The pointing was quite stable, with rms jitter of about 0".7 and no gradual drifts, except for one 30 s period when there was an excursion of about 10″. The photometric correction program tracked this excursion accurately, so the jitter correction for this period should be accurate as well.

CH Cyg.—The measured flux from this star varied gradually during the observation, rising and falling by almost 50%. The pointing was fairly stable, with rms jitter of 1″.2 and one shift of about 4″. The flux variations were not correlated with any changes in pointing, so the derived photometric correction of about 8% is probably not meaningful. The jitter corrections are probably reliable, and are small in any case.

EG And.—This star was observed twice in the mission. The first observation was obtained shortly after activation and was split into two exposures at different primary mirror focus positions to supplement the α Aur focus data obtained during activation. The pointing was rather unstable during the first observation, but the count rates calculated from the pointing errors by the photometric correction program matched the observed rates quite well, giving confidence in the results of the corresponding spectral jitter correction.

The final observation was obtained late in the mission, at the then nominal mirror focus offset of −100 μm. The pointing stability was somewhat better for this observation: the rms jitter was about 1″, and there were 3″–4″ steps (perpendicular to the dispersion direction) at the beginning and end of the observation that caused drops in flux of about 15%. These flux losses were tracked well by the photometric correction program.

RR Tel.—This was the only emission-line object bright enough to require observation through the 750 cm^2 door configuration. The airglow emissions were consequently relatively weak. The observation took place roughly two-thirds of the way through the mission, by which point the loss of detector response at Lyα was sufficient to cause an absorption trough to appear at line center. The pointing was stable throughout, with rms jitter of about 1″ and gradual drifts of 1″–2″.

V 1016 Cyg.—The rather large photometric correction factor results from the fact that the exposure interval includes part of the target acquisition period. The star is sufficiently bright that the airglow is relatively insignificant away from Lyα and O I 1304 Å, even though this was a day observation. The pointing stability was reasonable, with an rms jitter of 1″.0 in the dispersion direction and 1″.4 in the transverse direction. The star was offset by almost 4″ from the slit center, however, so that even this relatively small jitter gave rise to measurable fluctuations in count rate. These fluctuations were tracked well by the photometric correction program.

Z And.—The pointing was quite stable for this observation, with rms jitter of 0″.75 and drifts of about 1″ in the dispersion direction (1″.2 and 2″, respectively, in the transverse direction). The count rate was stable throughout.

A reduced spectrum for each of the wavelength or resolution calibration objects is shown in Figure 4. Only one exposure is shown for objects with multiple primary mirror positions, as the differences among the exposures are not visible on the scale of these figures.

4. CHANGES IN SENSITIVITY DURING MISSION

The instrument sensitivity declined during the mission. The amount of decline was greatest at short wavelengths

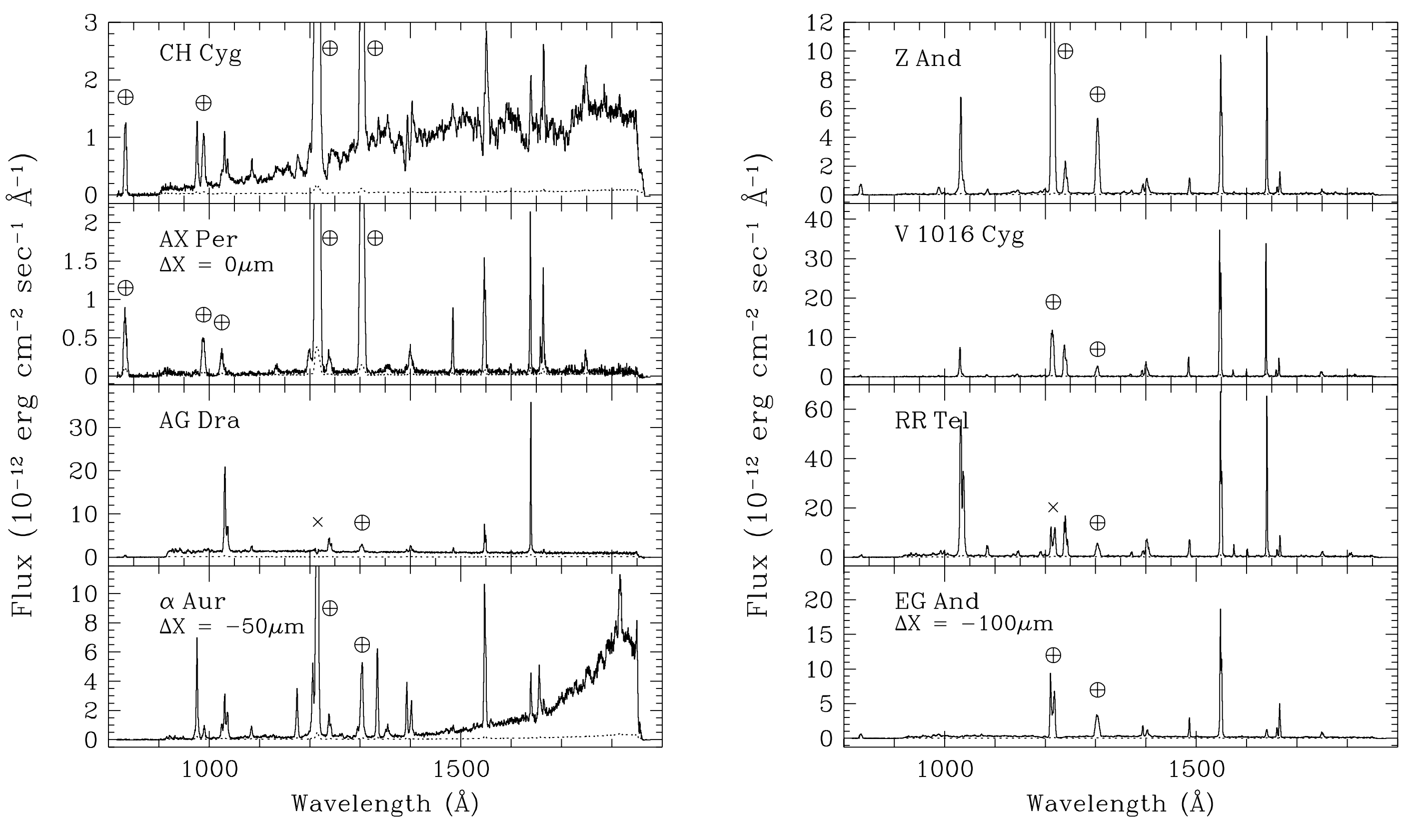

FIG. 4.—Reduced spectra of HUT wavelength and resolution calibration observations are shown as solid lines, the statistical errors as dashed lines. The spectra are unsmoothed and are sampled at 0.51 Å pixel^{-1}. Wavelengths at which significant geocoronal emission was present are marked with earth symbols, and spurious structure in the spectra arising from overexposure of the detector to airglow at 1216 and 1304 Å is marked with a cross (see text). Only a single spectrum is shown for those objects that had multiple exposures taken at different primary mirror focus positions.

(26% at 912 Å), least at long wavelengths (5% at 1840 Å), and varied monotonically in between. This decline was characterized by examining the spectra of the three DAs that were observed more than once during the mission: HZ 43, GD 394, and RE 1738+669. Each spectrum was fully reduced as described in the previous section, except that no corrections for time dependence were applied and the preliminary effective area was used. For each star the spectra obtained at earlier MET were divided by the spectrum obtained at the latest MET. Since the latest observation for each of these stars was obtained on the final day of the mission (329^h MET for HZ 43, 340^h MET for GD 394, and 347^h MET for RE 1738+669), the result is a family of curves describing the effective area at various times relative to the end of the mission. This characterization of changes in instrument sensitivity depends only on the stability of the stars themselves; there are no implicit assumptions concerning the intrinsic stellar fluxes. A good fit to the family of curves was obtained by the function

$$F(\lambda, t) = e^{-a(t)\sigma(\lambda)} ,$$

where

$$a(t) = \frac{t(\text{hours}) - 32.605}{196.417} \quad \text{for } t \le 229 ,$$

$$a(t) = 1 \text{ for } t > 229 ,$$

$$\sigma(\lambda) = -0.7522 + 7.7724 \times 10^{-4}\lambda - 2.1040 \times 10^{-7}\lambda^2 .$$

The resulting family of curves is shown in Figure 5. When the individual spectra for a given star are corrected with this fitted function and divided by one another, the residuals are comparable to the statistical errors and there are no systematic offsets or slope errors.

This correction factor is computed for each spectrum, with t being set to the MET at the start of the exposure. The same corrections are applied to spectra obtained through all door configurations.

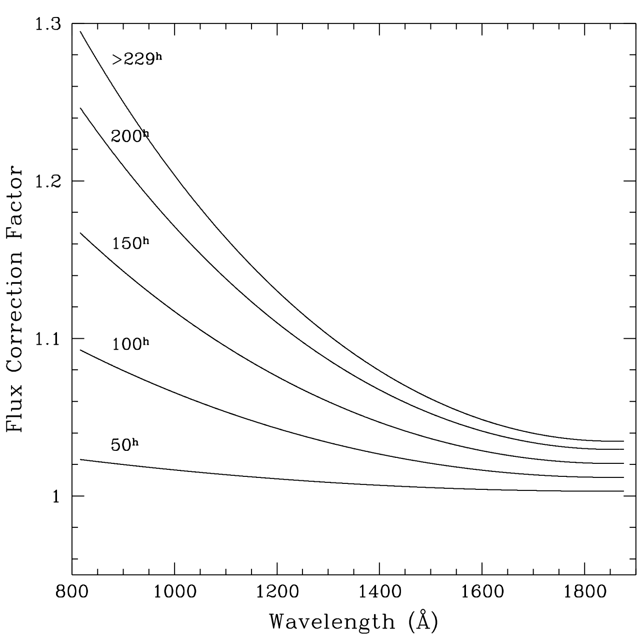

FIG. 5.—Family of curves giving corrections to the instrument inverse sensitivity for several values of MET are plotted as a function of wavelength. Each curve is labeled with MET in hours since launch. The degradation of the instrument sensitivity appeared to cease after about 229^h MET, so the uppermost curve applies through the end of the mission.

The overall wavelength dependence and time dependence of the change in throughput is suggestive of absorption by a contaminant on the telescope optics. An analysis of the witness mirrors leads to a similar conclusion. There were two witness mirrors mounted in the telescope. Both were mounted on the inside of the telescope housing facing radially inward: one was located in the mirror cell (just behind the primary mirror), and one was located near the spectrograph (near the open end of the telescope). The witness mirror in the primary mirror cell was well protected from the exterior environment, but the relatively long vent paths for this area made it very sensitive to any contaminants arising from the mirror focus mechanisms, wiring harness, paints, or other materials present in the mirror cell. The witness mirror located at the spectrograph was nestled between vanes of the internal light baffles and did not have a direct LOS to the exterior of the telescope. It was in close proximity to the spectrograph and its associated electronics and mechanisms. This mirror was therefore less sensitive than the primary mirror to external contaminants.

The witness mirrors were measured and installed in 1995 February; they were removed and remeasured in 1995 July/August. The surfaces were then examined by means of X-ray photoelectron spectroscopy to search for possible contaminants. The reflectivity of the witness mirror located in the mirror cell did not change, nor did it appear to be contaminated. The reflectivity of the witness mirror located at the spectrograph declined in a manner similar to the primary mirror but not by quite as much: 4.5% at 1608 Å, 13% at 1216 Å, and 18% at 1025 Å. This mirror was also found to have unidentified material on its surface, including fluorocarbons and something containing O—C=O and C=O functional groups.

Our tentative conclusion is that the instrument throughput declined because of contamination of the primary mirror and that the origin of the contaminant was in the shuttle environment rather than internal to the telescope.

5. DETECTOR PERFORMANCE

There are many aspects of the detector performance that influence the quality of the reduced spectra. These include the background events ("dark count"), spatial resolution and pixelization, readout rate, phosphor persistence, "flat-field" effects, and variations in gain.

5.1. *Dark Current*

There are two components to the background events: internal background, due primarily to trace quantities of radioactive elements in the MCP glass, and the radiation environment in low earth orbit. The background rate measured in the lab preflight was 1.88×10^{-4} counts s^{-1} pixel^{-1} (0.602 counts s^{-1} cm^{-2}) for a phosphor voltage setting of 3 and was uniform across the detector. The detector background in orbit was characterized by examining the data obtained during target acquisitions with the blank slit covering the spectrograph entrance. Nearly 75 ks of such data were obtained during the mission. The background rate outside of the SAA was 4.11×10^{-4} counts s^{-1} pixel^{-1} for a phosphor voltage setting of 3 (1.316 counts s^{-1} cm^{-2}), and 4.76×10^{-4} counts s^{-1} pixel^{-1} for a phosphor voltage setting of 4 (1.524 counts s^{-1} cm^{-2}). Orbit-to-orbit variations in the background were typically 20% of these mean values. When passing through the SAA the background rate increased to as much as 1.78×10^{-2} counts s^{-1} $pixel^{-1}$ (57 counts s^{-1} cm^{-2}). Wavelength-dependent structure in the dark current was examined by summing all of the available data for a given phosphor voltage and SAA level and binning the resulting "spectra" by 25 pixels. The SAA level was defined in seven intensity steps, ranging from zero outside of the SAA to six at the center of the SAA. All such spectra show a dip at Lyα resulting from exposure to the intense geocoronal emission during the mission. The summed dark current spectra obtained outside of the SAA are shown in Figure 6*a* for a phosphor level of 3 and in Figure 6*b* for a phosphor level of 4. The fluctuations of each bin about the mean are generally consistent with Poisson statistics. One possible exception is a $\gtrsim 3\ \sigma$ peak at about 990 Å in the phosphor level 3 spectrum. It should be noted that the dark current rate is sufficiently low that it averages less than 1 count $pixel^{-1}$ per 2000 s integration. Thus, for most circumstances, wavelength-dependent structure in the background at the level seen in Figure 6 is negligible. However, as pointed out by Hurwitz, Jelinsky, & Dixon (1997), when summing many adjacent pixels to determine detection limits, the bin-to-bin structure seen in these figures may be significant.

5.2. *Spatial Resolution*

The photodiode spacing of 25 μm imposes a regular pixelization on the detector readout. A typical event would distribute signal over 10–15 diodes, which would be centroided to half-diode precision. The resulting spectral pixels were 12.5 μm, which was equal to the center-to-center spacing of the MCP pores. The pore spacing determines the absolute lower limit to the detector resolution; larger scale structure in the MCP fiber bundles, trajectories of photoelectrons converted between pores, redistribution of the signal by the fiber optic window, and so on probably all combine to result in a net detector resolution closer to 20 μm. The contribution of the detector spatial resolution to the total instrumental line spread function is discussed in detail in § 15.

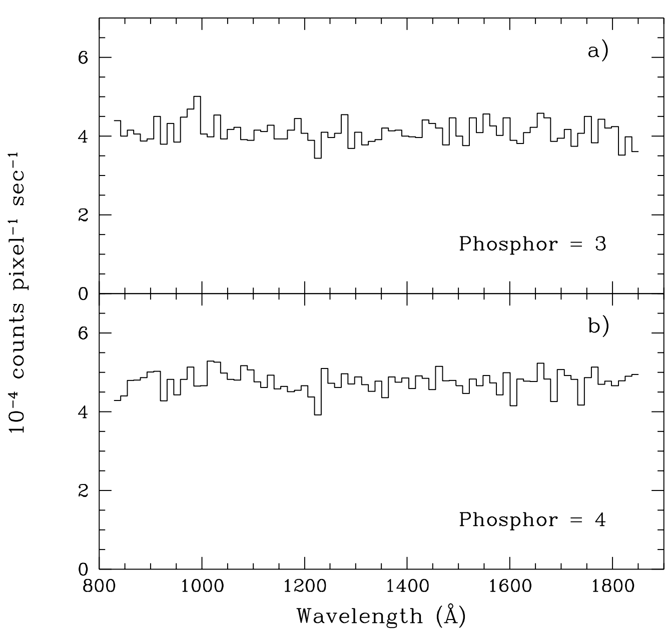

FIG. 6.—Mean dark count rate $pixel^{-1}$ outside of the SAA is plotted: (*a*) for a phosphor voltage setting of 3 and (*b*) for a phosphor voltage setting of 4. The dark rate has been binned over 25 pixels for plotting purposes.

5.3. *Dead Time*

The photodiode array provides a stable, distortion-free measurement of event position; however, the time required to read it out has a number of consequences. The photodiodes are digitized sequentially at a rate of 1 MHz, so a complete scan of the array requires 1.024 ms and each diode integrates the signal received between successive scans (a new scan begins immediately on the completion of the previous scan). The on-board Spectrometer Processor (SP) centroids the events found in each scan and increments the corresponding pixel in the spectrum. If two events occur during a scan that are physically close enough to illuminate overlapping clusters of diodes, the SP is unable to separate them. If the merged event satisfies the pulse height and pulse width criteria, the SP registers a single event at the combined centroid position. If the merged event fails either of these criteria it is rejected and all of the "detected" photons are lost. Corrections for these dead-time effects are calculated by a detailed Monte Carlo simulation of the detector response for each input spectrum. This Monte Carlo procedure is described in detail in Appendix B of Kruk et al. (1997).

The magnitude of the dead-time effects is affected by the pulse heights and pulse widths of events registered by the detector. The measured pulse heights and widths obtained during the mission were used to generate distribution functions for these quantities that varied with aperture door configuration, wavelength, detector voltage, and MET. The appropriate distribution functions were then used by the Monte Carlo program when computing the dead-time corrections for each spectrum.

The dead-time effects were negligible for most of the observations obtained with HUT during the mission. The maximum correction for a stellar source was ∼9%. The corrections for the Lyα or O I 1304 Å lines could easily reach 50% or more during the day, but the uncertainties in the corrections for loss of detector gain at these wavelengths causes the apparent fluxes in these lines to be unreliable after the first few days of the mission.

5.4. *Phosphor Persistence*

A second consequence of the detector readout time is the presence of events caused by phosphor persistence. If an event occurs at a cluster of diodes shortly before they are digitized, the phosphor can still be emitting light after the diodes are read out. The result is that some of the signal will be read out in the subsequent scan. If enough signal is present to be above threshold, the SP will detect a second event at the same location. Such a "persistence event" was measured to occur for 8% of all real events, independent of wavelength (there is a slight dependence on detector gain, but the wavelength-dependent effects are negligible). Because this is a constant multiplicative factor, it was simply absorbed into the definition of the effective area. An explicit correction is required for the statistical errors that are propagated during the data reduction, because the statistical error is the square-root of the number of detected photons, not the number of detected photons plus persistence events. Hence, the statistical errors were computed by dividing the measured number of events in a pixel by 1.08 and then taking the square root. These uncertainties were then propagated throughout the remainder of the data reduction process.

6. FLAT-FIELD CORRECTIONS

Flat-field features are fluctuations in the effective area of the instrument on wavelength scales of a few angstroms. By the end of the mission the HUT detector exhibited a number of such features, all in the form of localized depressions in the instrument sensitivity. Each such feature is attributable to degradation of the detector as a result of exposure to bright emission lines. Such exposure reduces the gain in the MCPs, shifting the pulse height distribution to lower pulse heights. Initially, the entire pulse height distribution remains above the detector threshold and no loss of sensitivity occurs. In most cases, the gain declined only to the point where a few percent of the distribution fell below the threshold. For the case of Lyα, however, the gain declined to the point where the majority of the distribution was below threshold. Three types of sources were responsible for these features: (1) calibration lamps (used preflight), (2) airglow, and (3) the Wolf-Rayet star HD 50896.

Two types of preflight activities resulted in flat-field features: alignment and focus of the spectrograph, and payload integration testing. The preflight spectrograph alignment and focusing activities frequently involved measurements of an argon spectrum containing strong lines at 1048 and 1067 Å. The payload integration testing required frequent use of a mercury lamp mounted on the spectrograph. This lamp was mounted so that the 1849 Å doublet appeared in the HUT spectrum at 1662.6 Å/1670.7 Å. Cumulative exposure to these lines produced flat-field features prior to the mission, which did not subsequently change in strength.

The intense airglow emissions at Lyα and O I 1304 Å significantly degraded the detector response over a period of days, as expected from our Astro-1 experience. By the end of the mission, the detector response at Lyα was almost nonexistent. The FWHM of the resulting apparent absorption features was $\lesssim 7$ Å, which slightly exceeds the widths of the airglow lines obtained through the 20″ diameter slit (through which most observations were obtained). Events in the affected regions would occasionally be miscentroided and give rise to weak peaks on either side of the apparent absorption. This is generally visible only for the 1304 Å feature in night spectra (e.g., the HZ 43 spectrum at 329^h MET), because at Lyα or at 1304 Å during the day these peaks are lost in the tails of the airglow emission. No attempt was made to correct spectra for the features at Lyα or 1304 Å. The uncertainties in such corrections would have been large, and it was deemed preferable to leave obvious defects that would alert the user to the presence of unreliable data at these wavelengths.

By the end of the mission, the O I 989 Å emission line also gave rise to a weak flat-field feature. This was treated as increasing linearly in strength from 134^h MET until the end of the mission.

The N I 1200 Å airglow emission most likely produced a feature in the detector similar to that at 989 Å. However, due to its proximity to Lyα, this feature was difficult to discern from the tails of the Lyα line and no correction was attempted.

The star HD 50896 (EZ CMa) was observed 4 times during the mission, through the 50 cm^2 door in all cases. Its spectrum is dominated by a number of strong broad emission lines, and the strongest lines caused corresponding dips in the detector response. This star was observed at 48^h, 72^h, 97^h, and 134^h MET. The first two observations do not appear to have reduced the detector gain sufficiently to cause any features, but following the observation at 97^h MET, features were observed at 1243, 1551, and 1641 Å (from the N V, C IV, and He II stellar wind lines, respectively). The strength of each of these features roughly doubled following the observation at 134^h MET. Since these features could be traced to specific times in the mission, corrections were applied accordingly: no correction was applied to spectra obtained before 97^h MET, a single correction was applied to all spectra obtained between 97^h and 134^h MET, and a second correction was applied for subsequent observations.

The strengths of the corrections were determined by examination of the spectra of a number of DA white dwarfs, which are expected to have featureless continua at the wavelengths in question. The observed spectra were divided by model spectra, and the residuals in the vicinity of the flat-field features were then fitted with Gaussian line profiles. The stars used for this purpose were HZ 43, GD 71, GD 153, GD 50, Wolf 1346, and GD 394 (not used for the 1550 Å feature). Whenever possible, residuals from spectra obtained at similar times in the mission were combined prior to fitting. Unfortunately, there were only a handful of DA spectra obtained over the time interval 48^h to 134^h MET when the observations of HD 50896 took place. The corrections for the features at 1243, 1551, and 1641 Å are therefore more uncertain in this time interval than is the case for the other corrections. The resulting positions, equivalent widths, and FWHMs of each feature are given in Table 3 as a function of MET. The nominal wavelengths of each feature are given, as well as the pixel number, but it should be noted that the locations of these features are fixed in pixel coordinates: the flat-field correction must be applied prior to any shifts of the spectrum needed to correct the wavelength scale for miscentering of the target in the spectrograph slit.

The same flat-field corrections are applied to spectra obtained through all door configurations, which may not be appropriate in all circumstances. Data to assess the strengths of the features were available primarily from spectra obtained through the full-aperture door. The results should apply to spectra obtained through the reduced aperture door configurations for the features induced preflight or by airglow, because the illumination causing the features was fairly uniform across the height of the detector active area. It might be reasonable to expect, however, that the features induced by the observations of HD 50896 would be stronger for reduced aperture observations. The HD 50896 observations were obtained through the 50 cm^2 door, which illuminates a much narrower region of the detector than the full-aperture door. The measurements of these particular flat-field features by means of full-aperture observations would therefore seemingly be diluted by illumination of unaffected regions of the detector.

There are three observations that can potentially provide a measurement of the reduced aperture flat-field features: the last GD 394 observation at 340^h MET, the LS V 46°21 observation at 320^h MET, and the observation of NGC

TABLE 3

Flat-Field Features: Equivalent Width versus MET

Pixel	λ (Å)	EW after MET (Å)[a] 0h	97h	134h	329h	FWHM
338.47	989.16	0.0	0.0	0.0	0.27	4.2
454.28	1048.82	0.40	0.40	0.40	0.40	5.9
489.15	1066.80	0.51	0.51	0.51	0.51	7.6
830.72	1243.41	0.0	0.14	0.29	0.29	4.8
1422.6	1550.97	0.0	0.16	0.31	0.31	5.2
1596.94......	1641.84	0.0	0.48	0.94	0.94	11.0
1636.73......	1662.59	0.81	0.81	0.81	0.81	8.3
1652.28......	1670.73	0.81	0.81	0.81	0.81	12.3

[a] Equivalent widths are constant between the times shown, except for the 989 Å feature, which increases linearly in strength after 134^h.

1360 at 308^h MET. The last GD 394 and LS V 46°21 observations each utilized both the full aperture and 750 cm^2 apertures in order to measure the relative sensitivities of the two door configurations. The ratio of the 750 cm^2 spectrum to the full-aperture spectrum was computed for each star and examined for residual flat-field features. These ratios were rather noisy, but in each case the ratio appeared to show dips at 1243, 1551, and 1641 Å that were roughly comparable to the values given in Table 3, indicating that these features were roughly twice as strong in the 750 cm^2 spectra as in the full-aperture spectra. Unlike these two observations, the observation of NGC 1360 was designed explicitly to measure flat-field features for the 750 cm^2 door configuration. Following the target acquisition, the HUT mirror was used to offset the star within the spectrograph slit, thereby shifting the spectrum by 6 pixels. Figure 7 shows the first spectrum overplotted with the second spectrum, after the latter has been shifted by 6 pixels to the red. An uncorrected feature will appear as a depression of the earlier spectrum relative to the second at the pixel in question, and a matching depression of the second spectrum relative to the first 6 pixels to the red. The full-aperture flat-field corrections were applied to both spectra prior to shifting. The uncorrected features at Lyα and 1304 Å show up clearly. There appears to be a small residual mismatch at N v, but the spectra are clearly well matched at C iv and He ii 1640 Å. There is also an apparent feature at pixel 234 (corresponding to a wavelength of 936 Å). A fit to this feature gives an equivalent width of 0.72 Å and an FWHM of 5.3 Å. This feature is apparent in neither the GD 394 nor the LS V 46°21 750 cm^2 exposures mentioned above, nor is it seen in the G191-B2B spectrum.

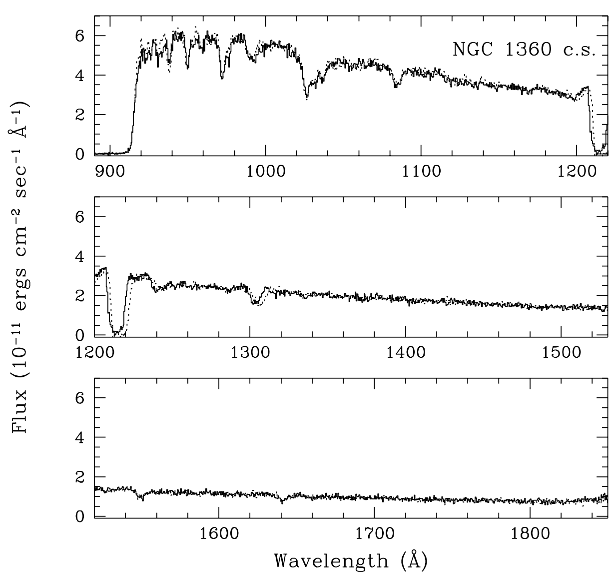

Fig. 7.—First spectrum of NGC 1360 is shown as the solid line; the second spectrum, obtained with the star offset within the slit relative to the first exposure, is overplotted as a dotted line after first shifting it 6 pixels to the red. Both spectra have had airglow and nebular emissions subtracted, and both were corrected for full-aperture flat-field features. The uncorrected features at Lyα and at 1304 Å are readily apparent. The uncorrected feature at 936 Å is also visible (see text).

The lack of consistency between the various measurements of flat-field effects for the reduced aperture observations made it difficult to decide on the best means of correcting for them. It was not expected prior to the mission that the flat field would vary with time (other than at Lyα and 1304 Å), so proper calibration observations were not planned for this purpose. In any case, the astigmatic image height on the detector for the reduced aperture observations is sufficiently small that it is comparable to the dimensions of the 20″ slit, especially at short wavelengths. As a consequence, placement of the target star within the slit may influence the effective flat-field correction required (for those features induced by observations through the same door configuration only, i.e., for the 1243, 1551, and 1641 Å features). We chose therefore to apply the full-aperture flat-field corrections listed in Table 3 to all the archived spectra, with the caveat that this may undercorrect the spectra obtained through the 750, 200, and 50 cm^2 doors by as much as a factor of 2 at 1243, 1551, and 1641 Å. In addition, it is possible that there is an uncorrected feature at pixel 936 Å for these door configurations.

7. WHITE DWARF MODEL SPECTRA

7.1. *Discussion of the Model Code*

The spectra for the calibration were calculated using Detlev Koester's white dwarf model atmosphere codes, which are described in full detail by FKB. The models assume plane-parallel geometry and local thermodynamic equilibrium. Given that these models are used for the instrument calibration through the full Lyman series, two important factors are the treatment of hydrogen line broadening and of line and continuum opacities.

Stark broadening of the Balmer and Lyman lines is based on the unified theory of Vidal, Cooper, & Smith (1973, hereafter VCS), using extensive tables (up to $n = 22$) recently calculated by Lemke (1997). The treatment of line and continuum opacities is essentially the same as that presented by Däppen, Anderson, & Mihalas (1987) and is based on the Hummer-Mihalas occupation probability formalism (Hummer & Mihalas 1988; Mihalas, Däppen, & Hummer 1988). In the Hummer-Mihalas formalism, pressure ionization of a given level is assumed to occur when the strength of the electric field due to adjacent perturbers exceeds a certain critical strength F_c (eq. [4.23] of Hummer & Mihalas 1988). The probability of a given level being "dissolved" then depends on the distribution of field strengths. Under this scenario, photoabsorption may occur via a transition from a given level to a higher level, or to a free state, or to a "dissolved" level that is neither truly bound nor truly free. The latter type of transition forms a "pseudocontinuum" that overlies the line series.

Our treatment differs from that of Däppen et al. (1987) in two respects. A minor difference is that Däppen et al. (1987) calculated the pseudocontinuum cross section longward of the unperturbed ionization edge by extrapolation of the bound-free absorption cross section. Our approach is to simply assume a constant cross section, equal to the value at the ionization edge. Given that the pseudocontinuum opacity is greatest among the higher lines and weakens rapidly toward longer wavelengths, the two methods should be essentially equivalent.

More importantly, as noted by Däppen et al. (1987) and by Bergeron (1993), the VCS theory predicts line wings that are too strong where they overlap significantly. This is because VCS only considers two levels at a time, which cannot be valid where the lines overlap. A solution to this problem, proposed by Bergeron (1993) and which we have adopted, is to increase the critical field strength somewhat, reducing the pseudocontinuum opacity to compensate for the line wing opacity being too strong. Bergeron found that increasing the critical field strength by a factor of 2 resulted in emissivities that matched the laboratory data for the Balmer series from Wiese, Kelleher, & Paquette (1972) and also gave consistent fits to observed Balmer line profiles in DA white dwarfs. The present work shows that the critical field strength adjustment also produces the correct model fluxes throughout the Lyman line region for DA white dwarfs in the 30,000–60,000 K range. The implications of that result for hydrogen line and continuum opacities in the Lyman and Balmer line regions will be presented in a forthcoming paper (Finley et al. 1999).

7.2. *Model Spectra Used for the Calibration*

The code described above was used to calculate the emergent spectra for the stars HZ 43, GD 71, GD 153, and G191-B2B. The atmospheres were assumed to be pure hydrogen, which is an excellent approximation for the first three stars (other constituents are undetectable even in EUV spectra; Dupuis et al. 1995). G191-B2B is known to contain trace quantities of heavy elements, but Kruk et al. (1997) demonstrated that pure hydrogen models provide satisfactory results for this star in the HUT first-order wavelength range. The effective temperatures and surface gravities used were those determined by FKB from fits to Balmer line profiles, and the resulting model spectra were normalized by the measured V magnitudes of the stars using the relation $F_\lambda(5490\ \text{Å}) = 3.61 \times 10^{-9} \times 10^{-0.4V}$. This normalization is within 0.5% of that adopted for the white dwarf models used to define the calibration of *HST* FOS and STIS; normalization issues are discussed in greater detail by Kruk et al. (1997).

The model fluxes were corrected for attenuation by H I and He I in the interstellar medium. The column densities of Dupuis et al. (1995) were used for GD 71 and GD 153; the average of the column densities reported by Dupuis et al. (1995) and Kimble et al. (1993a) were used for G191-B2B, and the average of the column densities reported by Dupuis et al. (1995) and Kimble et al. (1993b) were used for HZ 43. Atomic data used for computing the interstellar absorption were taken from the compilation of Morton (1991); values for H I Lyman lines 13–49 were calculated by one of us (G. A. K.). Doppler b-values were set to a nominal 10 km s^{-1}. This is consistent with the value of 11 km s^{-1} measured by Hurwitz & Bowyer 1995 for G191-B2B; a value of about 15 km s^{-1} would have given a better match to the observed position of the Lyman edge for the other three stars but would have little other effect on the spectra. The interstellar absorption was calculated in the vicinity of each interstellar line at a variable resolution fine enough so that linear interpolation of the resulting table would give errors of less than 1%, and the stellar model was then interpolated at each of these wavelength points. The interstellar absorption was also calculated for every wavelength point in the stellar model, and the two lists of stellar flux times interstellar transmission were then merged.

The model flux shortward of about 950 Å is also corrected for attenuation by the upper atmosphere of the earth. Column densities for O, O_2, and N_2 along the LOS for each observation were obtained from the MSISE-90 (mass spectrometer incoherent scatter model-extended) models of the atmosphere (Hedin 1987), using the on-line computational model available at Goddard Space Flight Center[5]. The latitude, longitude, and altitude of the space shuttle during the observations of each white dwarf were accounted for, as was the variation in earth limb angle during each observation and the degree of solar activity at the time of each observation. Because the mission took place at solar minimum and because the target visibilities were such that the exposure time was obtained primarily at large earth limb angles, this correction was negligible (less than 0.5% for the first-order flux).

The resulting spectrum was then convolved with the Gaussian instrumental resolution function described by Kruk et al. (1995), whose width varies with wavelength (2–4 Å). This smoothed spectrum was resampled on the HUT wavelength scale for direct comparison with the observed spectra. Note that the resolution function taken from Kruk et al. (1995) is generally broader than the more recently determined values given in § 15 for full-aperture observations. Because we have deliberately ignored the resulting bumps in the effective area at the Lyman lines, this should have no effect on the final results (see § 8).

The stellar model parameters and interstellar column densities utilized in the model flux calculations are listed in Table 4. These model parameters differ only slightly from those used to calculate the models that defined the final

[5] See also, http://envnet.gsfc.nasa.gov.

TABLE 4

WHITE DWARF MODEL PARAMETERS

Star	T_{eff} (K)	log g	V	log N(H I)[a] (cm^{-2})	log N(He I)[a] (cm^{-2})
HZ 43	50900	8.00	12.914	17.88	16.78
GD 71..........	32750	7.68	13.032	17.80	16.72
GD 153	38700	7.66	13.346	17.99	16.82
G191-B2B......	61200	7.50	11.781	18.26	17.16

[a] Column density of interstellar material.

HST FOS calibration (Bohlin et al. 1995), which were based on a preliminary version of the FKB results. The uncertainties quoted by FKB for T_{eff} are ± 640 K for HZ 43, ± 92 K for GD 71, ± 150 K for GD 153, and ± 241 K for G191-B2B. These are the formal errors; the actual accuracy is closer to ± 1000 K for HZ 43 and G191-B2B, and ± 500 K for GD 71 and GD 153.

The value of T_{eff} in the present model for G191-B2B is 2050 K hotter than the value used to define the Astro-1 HUT calibration. This leads to the new model flux being greater than the old by 1% at 1860 Å, 2.3% at 1000 Å, and 7% at the Lyman edge. The value for T_{eff} determined from the laboratory calibration of the Astro-1 HUT instrument ($T_{eff} = 62{,}100$ K; Kruk et al. 1997) is actually in better agreement with the present model value than with the earlier value.

8. SENSITIVITY FOR FULL-APERTURE OBSERVATIONS

The full-aperture sensitivity of the Astro-2 HUT instrument is defined by model atmosphere calculations for three stars: HZ 43, GD 153, and GD 71. The use of multiple stars reduces the effects of uncertainties in the model parameters for any one star. In addition, because the strengths of the Lyman lines differ substantially among these stars, the effects of uncertainties in the instrument spectral resolution are also minimized.

The spectra were reduced as described in § 3.1, steps 1–12. In addition, each spectrum was corrected for the changes in relative instrument throughput as a function of MET, as described in § 4. The variations in throughput versus MET were calculated solely from ratios of spectra of a given star at various times in the mission, so no implicit assumptions concerning model atmosphere parameters or anything else are involved. The result for each observation was a fully corrected count rate spectrum. Dividing the model atmosphere flux spectrum by the count rate spectrum for that star gives the inverse sensitivity curve of the instrument. If the energy per photon at each spectral pixel is divided by the inverse sensitivity and the (slightly variable) spectral width of that pixel, the result is the effective area as a function of wavelength. The effective area was derived separately from each of the observations, with statistical errors propagated at each step. The final effective area was then computed from the mean of the individual determinations, with each point weighted by its statistical error. Results from the first HZ 43 pointing only were used in the immediate vicinity of Lyα and 1304 Å, because the detector had not yet been affected by airglow at these wavelengths at the time of this exposure. The final effective area is shown in Figure 8.

The measured effective area was fitted with a cubic spline for subsequent use. The small peaks in the effective area that coincided with the positions of Lyman lines were obviously artifacts arising from errors in the cores of the line profiles and were excluded from the fit. The effective area varied smoothly with wavelength away from the cores of the Lyman lines, with one exception: a small (3%) bump at 985 Å and a shallow (2%) dip at 992 Å. This bump/dip structure appeared in all five individual measurements of the effective area and was therefore deemed to be an instrumental artifact. This structure was incorporated into the effective area, but could easily have been incorporated into the flat-field correction instead. The effective area was originally fitted with a 30 piece cubic spline over the entire wavelength range. This fit worked well except in the immediate vicinity of the bump/dip at 985/992 Å and at the relatively abrupt change in slope just longward of 1000 Å. As a result, an effective area curve was constructed by using this overall fit longward of 1045 Å, a separate 20 piece cubic spline fit was used for 915–1045 Å (except for the bump/dip structure), and the bump/dip structure itself was represented simply by

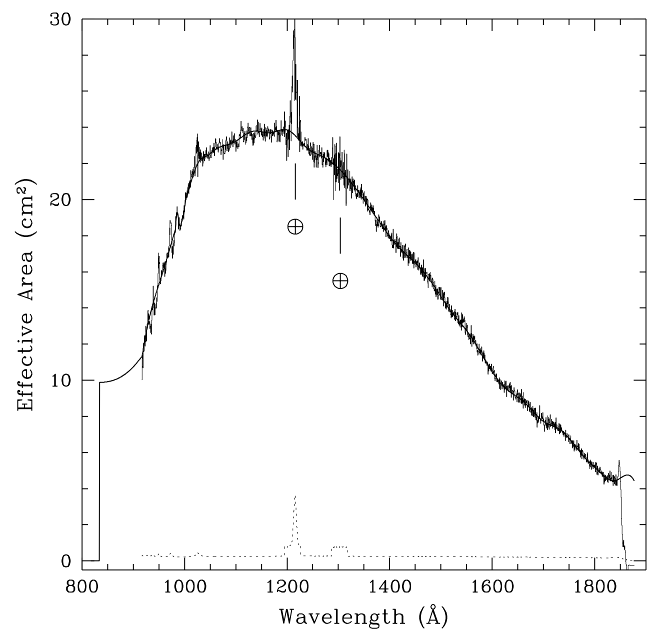

FIG. 8.—Measured first-order effective area for the Astro-2 HUT instrument is plotted as the thin (noisy) solid line; the statistical errors are plotted as the dotted line. The thick (smooth) line is the adopted effective area calibration. Longward of 912 Å the effective area was determined by comparison of in-flight measurements of HZ 43, GD 153, and GD 71 to model fluxes. Shortward of 912 Å the effective area is defined by the preflight laboratory calibration. The peak at Lyα is caused by residual airglow in the spectra used to derive the effective area. The measured area is noisy in the vicinity of 1304 Å because the only data used at these wavelengths were from the first HZ 43 observation, before exposure to airglow affected the detector response there.

the measured data after smoothing with a 9 pixel boxcar. This final curve is shown as the heavy solid line in Figure 8. This final curve differs from the single 30 piece spline fit by at most 2%, usually much less.

9. SENSITIVITY FOR REDUCED APERTURE OBSERVATIONS

The sensitivity calibrations for the various reduced aperture sizes were determined relative to the full-aperture calibration by means of repeated observations of a star through two different door openings. In all cases, both observations of a star through the two door configurations were obtained during a single half-orbit telescope pointing. The 750 cm^2 aperture was also calibrated directly by an observation of G191-B2B.

The 750 and 200 cm^2 door openings have a potential systematic uncertainty in the sensitivity calibration that is not present for the other door openings. The geometric areas of the full-aperture, half-aperture, and 50 cm^2 aperture door openings are fixed by the dimensions of the door frames: the door mechanisms are operated until a limit switch is tripped, ensuring that the opening is completely unobstructed. The 750 and 200 cm^2 openings are obtained by operating the motor for one of the two large doors for a fixed length of time (60 and 37 s, respectively), thereby uncovering a portion of the aperture. The opening time is governed by software in response to interrupts generated by a 4 Hz clock. The resulting inherent uncertainty in the opening time of 0.25 s corresponds to an uncertainty in the open area of 1% for the 750 cm^2 opening and 2.5% for the 200 cm^2 opening. However, there are two factors other than clock time that may result in larger uncertainties: temperature extremes at the relatively exposed door mechanism may alter the effective start-up time of the mechanism, and conflicts in software task scheduling may delay servicing of the clock interrupt. Low mechanism temperatures would potentially reduce the effective opening time of the door, while delays in interrupt servicing could increase the opening time (although it would be unlikely to increase it by more than one additional clock tick, or 0.25 s). We have no evidence that either of these effects actually occurred, but there is the potential that the true uncertainty may be somewhat larger than 0.25 s. This uncertainty, if present, only affects the absolute normalization of the spectra: the shape of the spectra would be unaffected.

9.1. *Half-Aperture* (2560 cm^2)

The effective area of the half-aperture door opening relative to the full aperture was measured twice: once with an observation of HZ 43 and once with an observation of GD 153. In each case the observation commenced with an exposure obtained through the full aperture. After roughly one-third of the observing time had passed, the door on the "$-Y$" side of the instrument was closed and the half-aperture exposure filled the remainder of the time. This gave roughly equal S/Ns in the two exposures. Each spectrum was reduced using the procedure described in § 3.1, through step 12. The resulting half-aperture count rate spectrum was divided by the corresponding full-aperture spectrum. These ratios are shown plotted in Figure 9. The ratios are fairly flat from 900 to 1400 Å and then roll over, declining by about 15% at 1800 Å. The two ratios are similar in shape and magnitude, differing from one another by 3% rms. The two ratios were therefore averaged and fitted with a three-piece cubic spline, which is shown as the smooth curve in

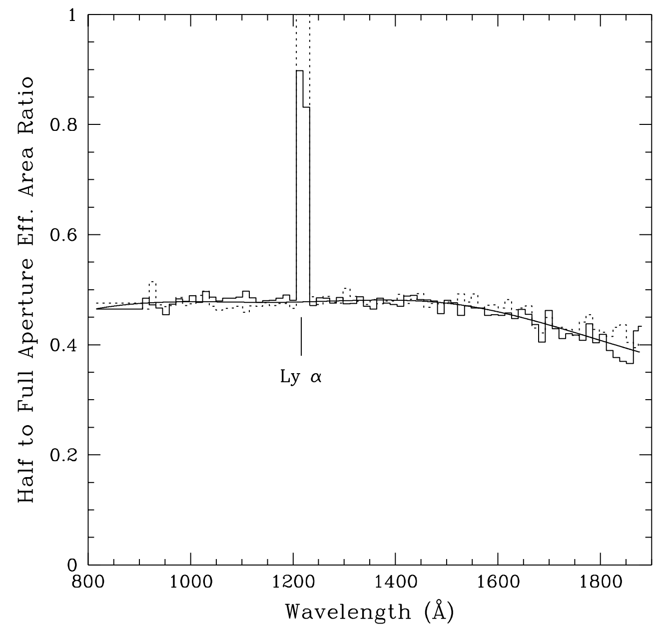

FIG. 9.—Ratio of the half-aperture to full-aperture effective area is shown. The solid histogram is the measurement obtained from an observation of HZ 43, and the dashed histogram is the measurement obtained from an observation of GD 153. The ratios were binned by 25 pixels for clarity. The smooth curve is a three-piece cubic spline fit to the average of the two measurements.

Figure 9. This spline fit was then multiplied by the full-aperture effective area to produce the half-aperture effective area and corresponding inverse sensitivity curves.

9.2. 750 cm^2 *Aperture*

The calibration of this aperture was performed by two independent means: measurements of a given star through both the full aperture and the 750 cm^2 aperture and direct calibration against a model of the DA white dwarf G191-B2B. The first approach was attempted in four separate observations: The GD 394 observations at 92^h, 138^h, and 340^h, and the LS V 46°21 observation at 320^h. The 750 cm^2 exposures in the first two GD 394 observations gave results that were consistent with the G191-B2B measurement, but they were too brief to be useful over much of the wavelength range and were therefore discarded. The third 750 cm^2 GD 394 exposure and the LS V 46°21 exposure were successful, and the resulting ratios of effective area relative to the full aperture are shown in Figure 10. The two ratios are similar in shape but differ by roughly 15% in magnitude. The observation of G191-B2B was used to determine the effective area of the 750 cm^2 aperture in the same manner as described above for the full-aperture calibration. The ratio of this effective area to the full-aperture area is also shown plotted in Figure 10. The wavelength dependence is similar to the other two ratios, and it falls between them in magnitude.

The effective area ratio derived from the G191-B2B observation was equal to the average of the LS V 46°21 and GD 394 ratios for wavelengths of 1100–1500 Å and gradually fell below it by 5% at 1840 Å and by up to 10% at the Lyman edge. Since the ratio derived from the G191-B2B observation had the greatest S/N, we used it to define the sensitivity calibration for the 750 cm^2 door opening. We did not use the effective area derived directly from comparison

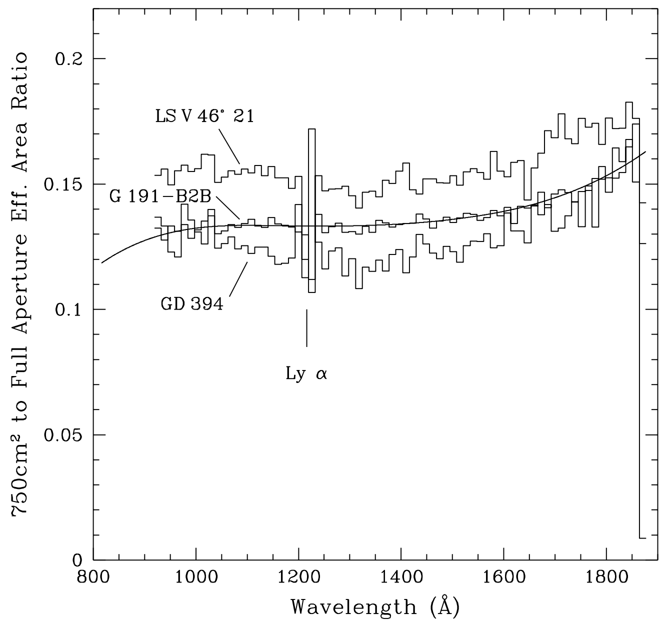

FIG. 10.—Ratio of the 750 cm^2 aperture to full-aperture effective area is shown. The upper histogram is the measurement obtained from an observation of LS V 46°21, and the lower histogram is the measurement obtained from an observation of GD 394. Both are direct comparisons of the fluxes measured through the two different door configurations. The middle histogram is the measurement obtained from an observation of G191-B2B by comparison with the model flux for that star. The ratios were binned by 25 pixels for clarity. The smooth curve is a three-piece cubic spline fit to the G191-B2B measurement.

of the observation to the model, however. Instead, we followed the same prescription used for the other reduced aperture calibrations: we took the ratio of the 750 cm^2 to full-aperture effective areas, fitted it with a three-piece cubic spline (*smooth solid line*, Fig. 10), and then multiplied by the full-aperture effective area to obtain the effective area for the 750 cm^2 door opening.

The magnitude of the offsets among the three measurements of the 750 cm^2 door effective area relative to that of the full-aperture door is difficult to explain. The pointing and count rates were quite stable throughout all three observations, so it is improbable that the differences were caused by placement of the stars too close to the edge of the slit. The observations of GD 394 and LS V 46°21 occurred at similar times in the mission, so the discrepancy cannot be explained by possible errors in the corrections for instrument degradation. The simplest explanation is that the door was not opened by the same amount for each observation. We had not planned any observations for the explicit purpose of testing the repeatability of the partial door openings. However, there were two objects that were observed repeatedly through the 750 cm^2 door opening. The stars HD 191765 and HD 96548 were each observed on three successive orbits, with the aperture doors being reopened to the 750 cm^2 position for each pointing. For HD 191765 the measured fluxes differed from the mean value by 0.2%, 0.4%, and 0.6%. For HD 96548, the measured fluxes differed from the mean value by 1.2%, 2.5%, and 1.7%. These results are slightly better than expected for HD 191765 and slightly worse than expected for HD 96548. Since these are Wolf-Rayet stars, however, intrinsic variations in the stellar flux of this magnitude would not be surprising, even on these timescales. In these tests the door openings were quite repeatable; nevertheless, based on the results shown in Figure 10, the absolute fluxes of spectra obtained through the partial door openings have an apparent systematic uncertainty of about 8% in addition to that of the full-aperture calibration.

9.3. 200 cm^2 *Aperture*

The sensitivity calibration for the 200 cm^2 aperture was determined by comparison with the 750 cm^2 aperture. The star G191-B2B was observed through both of these door configurations, and the ratio of the reduced count rate spectra was computed. This ratio was fitted with a three-piece cubic spline, which was multiplied by the effective area for the 750 cm^2 door opening to obtain the effective area for the 200 cm^2 opening. The ratio of the two spectra and the spline fit are shown plotted in Figure 11. This ratio shows very little wavelength dependence, as expected because these two door configurations differ little in how they illuminate the detector. The mean value of the ratio is 0.275, which is quite close to the nominal value of 0.267.

9.4. 50 cm^2 *Aperture*

The sensitivity calibration for the 50 cm^2 aperture was determined by comparison with the 200 cm^2 aperture. The star BD +75°325 was observed through both of these door configurations, and the ratio of the reduced count rate spectra was computed. This ratio was fitted with a three-piece cubic spline and multiplied by the 200 cm^2 effective area to obtain the effective area for the 50 cm^2 door opening. The measured ratio and the spline fit are shown in Figure 12. The ratio is fairly flat: it decreases slightly with decreasing wavelength, and declines a bit more steeply at the Lyman edge. The mean value is about 0.27, which is close to the nominal value of 0.25.

The sensitivity calibration for this aperture door configuration is the furthest removed from the white dwarf–derived calibration of the full aperture. In order to test this cali-

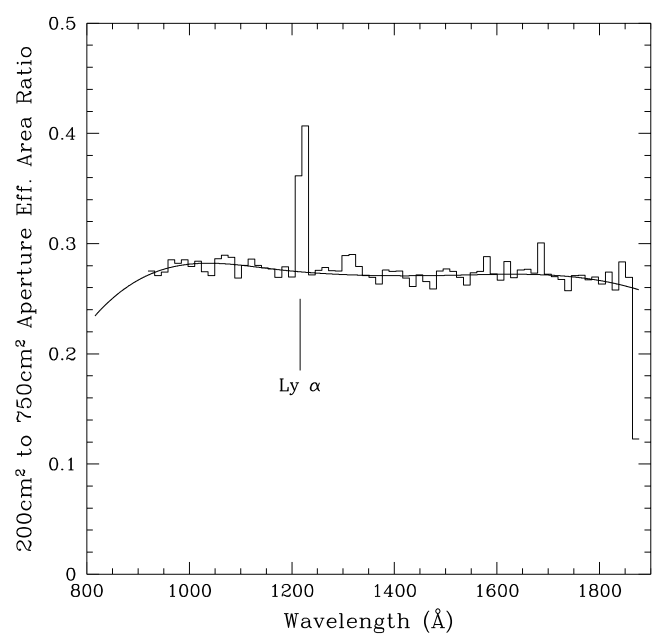

FIG. 11.—Ratio of the 200 cm^2 aperture to the 750 cm^2 aperture effective area is shown. The histogram is the measurement obtained from an observation of G191-B2B. The ratio was binned by 25 pixels for clarity. The smooth curve is a three-piece cubic spline fit to the measurement.

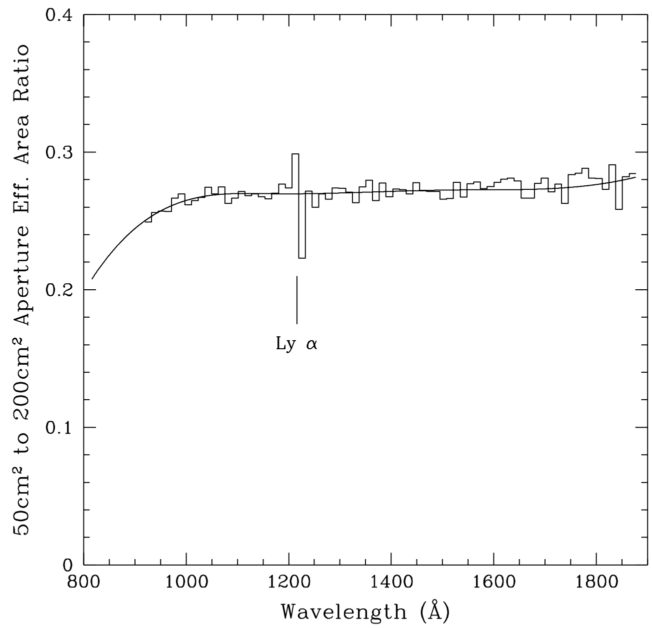

FIG. 12.—Ratio of the 50 cm^2 aperture to the 200 cm^2 aperture effective area is shown. The histogram is the measurement obtained from an observation of BD +75°325. The ratio was binned by 25 pixels for clarity. The smooth curve is a three-piece cubic spline fit to the measurement.

bration, we have compared the HUT spectrum of BD +75°325 to the *HST* FOS spectrum (kindly provided by Ralph Bohlin). These spectra are overplotted in Figure 13*a*, and the ratio of the HUT spectrum to the FOS spectrum is plotted in Figure 13*b*. This ratio increases smoothly from 0.95 at short wavelengths to 0.99 longward of about 1600 Å, apart from the dip in the HUT spectrum at Lyα caused by exposure of the detector to airglow emission.

10. SENSITIVITY IN SECOND AND THIRD ORDER

The HUT instrument has significant sensitivity at wavelengths corresponding to second- and third-order diffraction from the grating (407–920 Å and 271–613 Å, respectively). The use of SiC coatings substantially reduced the higher order response relative to the Astro-1 instrument, but there is still the potential for confusion from overlapping orders. For most HUT observations, of course, the interstellar medium blocks all flux shortward of 912 Å. However, for the nearest stars (including the white dwarfs used for the calibration) and for solar system objects the higher order flux must be accounted for.

The second- and third-order sensitivity was measured in the laboratory prior to the mission; no attempt was made to measure it in flight. The laboratory calibration measurements were performed in much the same way as for the Astro-1 postflight calibration, as described by Kruk et al. (1997). The calibration procedures will be described here only in cases where they differ from the Astro-1 procedures. The primary mirror reflectivity and spectrograph throughput were measured separately, and the results were combined to produce the overall instrument sensitivity.

The primary mirror reflectivity was measured in exactly the same manner as the Astro-1 mirror; the results are shown in Figure 14. Below 580 Å, the values shown are those of Kortright & Windt (1988), scaled by 0.9 because their data below 1000 Å are roughly 10% higher than for our mirror. The Astro-1 mirror reflectivity is also plotted for comparison. The reflectivity of the Ir-coated Astro-1 mirror only drops gradually at EUV wavelengths, while the reflectivity of the SiC-coated Astro-2 mirror drops precipitously shortward of 600 Å.

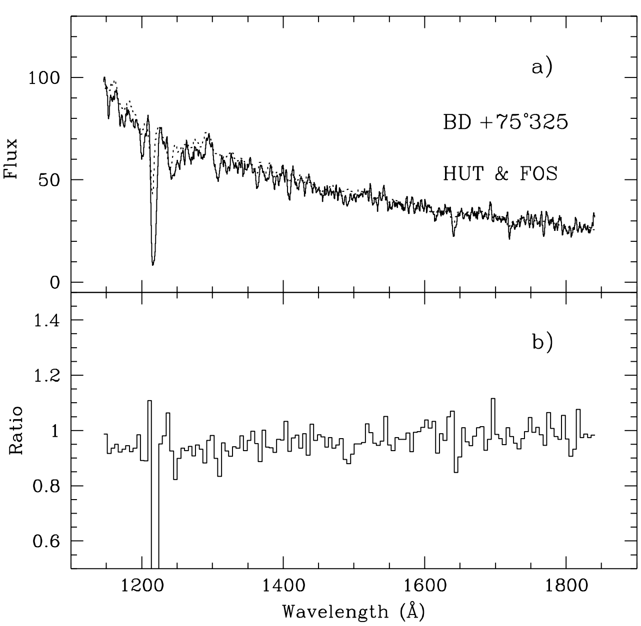

FIG. 13.—(*a*) HUT spectrum of BD +75°325 obtained through the 50 cm^2 aperture door is plotted as the solid line, and the FOS spectrum has been overplotted as the dotted line. The HUT spectrum was smoothed by 5 pixels for purposes of clarity. The flux is plotted in units of 10^{-12} ergs cm^{-2} s^{-1} $Å^{-1}$. (*b*) The ratio of the HUT spectrum to the FOS spectrum is shown, after binning by 10 pixels.

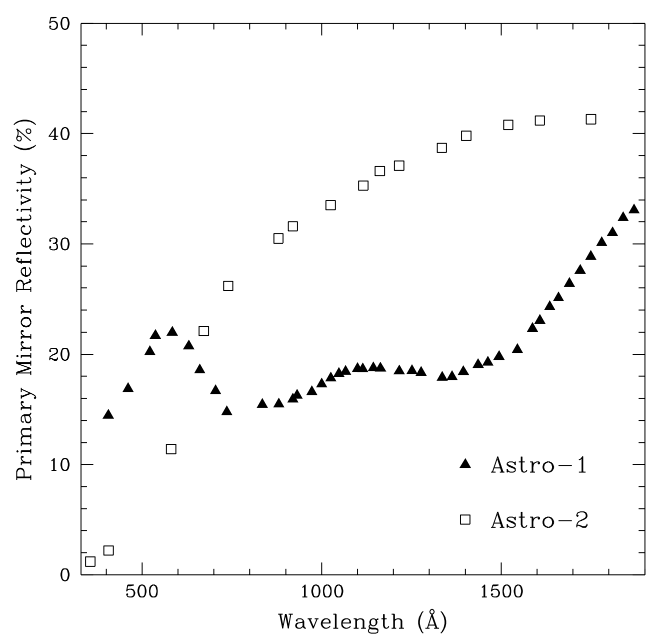

FIG. 14.—Measured reflectivity of the SiC-coated Astro-2 primary mirror is shown plotted as the open squares. The reflectivity of the Astro-1 primary mirror (Ir coating) is shown for comparison, plotted as the solid triangles. The SiC coating provides much higher reflectivity than Ir longward of 900 Å, but much less shortward of 700 Å.

The spectrograph throughput was measured by two means: in the Johns Hopkins University (JHU) calibration facility (which uses emission-line light sources) and at the Synchrotron Ultraviolet Radiation Facility (SURF) at the National Institute of Standards and Technology. The JHU measurements were performed in the same manner as for Astro-1, but the techniques for the SURF measurements were quite different from the Astro-1 measurements. These differences are described briefly here. As for the Astro-1 calibration, the spectrograph was mounted in the large gimbals in the vacuum tank at SURF so that the slit was at the center of rotation. This time, the motor drives on the gimbals were removed, and the gimbals were attached to linear feedthroughs mounted on vacuum flanges. This permitted rotation of the spectrograph so that the angle of the incident light relative to the spectrograph optical axis spanned nearly two-thirds of the *f*/2 cone of the HUT optics, instead of the much more limited range ($\pm 3°$) possible for the Astro-1 measurements. The synchrotron was operated with stored beam currents of only a few microamps to keep the detector count rate within acceptable limits. SURF produces a smooth continuum with usable flux from as short as 40 Å through the near IR. This gives rise to substantial problems with confusion of overlapping diffraction orders in the spectrograph being measured. For the Astro-1 measurements this was addressed by varying the energy of the circulating electron beam in order to change the relative contribution of the different orders. For the Astro-2 spectrograph measurements the synchrotron was operated at its standard energy of 284 MeV, and we attempted to perform order separation by means of bandpass filters. Two identical sets of filters were installed in series in the photon beam line. Each set of filters consisted of an LiF filter, an indium filter, and a tin filter, mounted in a "ladder" type holder on a linear vacuum feedthrough oriented perpendicular to the photon beam. For spectral pixels where a given type of filter transmits wavelengths corresponding to only a single diffraction order, the measured count rate in that pixel is

$$C_1 = F_\lambda T_\lambda^1 E_\lambda , \quad C_2 = F_\lambda T_\lambda^2 E_\lambda , \quad C_{12} = F\lambda T_\lambda^1 T_\lambda^2 E_\lambda ,$$

where T_λ^1 is the transmission of the first filter at wavelength λ, T_λ^2 is the transmission of the second filter at wavelength λ, F_λ is the synchrotron flux at wavelength λ, E_λ is the spectrograph efficiency at wavelength λ in the diffraction order being measured, and C is the count rate in the given pixel corresponding to wavelength λ in the diffraction order being measured. Placing first one filter in the beam, then the second filter, and then both filters permits determination of T_λ^1, T_λ^2, and E_λ. The aluminum filter mounted in the spectrograph slit wheel (the only filter present in HUT that can be inserted in the UV light path) could also be rotated into the light path in order to measure its transmission.

The In and Sn filters were 1600 Å foils on a 70 lines mm^{-1} nickel mesh backing, fabricated by Luxel. The LiF filters were 1 mm thick and were supplied by Acton Research Corporation. The foils were shipped in nitrogen-filled sealed bags and maintained in vacuum continuously, apart from a period of about 30 minutes while they were transferred from their bags into the holders. The LiF filter bandpass is $\lambda > 1000$ Å, producing a pure first-order spectrum. The In filter bandpass is 740–1075 Å, producing a nonoverlapping set of first- and second-order spectra: 814–1075 Å in first order and 740 − 920 Å in second order (occupying the pixels that correspond to 1480–1840 Å in first order). The In filters did transmit weakly shortward of 740 Å but not down to 538 Å (where it would have contaminated the first-order portion of the spectrum). The data obtained shortward of 740 Å were not used in the analysis. The Sn filter bandpass is 517–850 Å, but with some relatively weak but not insignificant transmission extending shortward of the abrupt edge at 517 Å. The Sn-filtered spectra were more difficult to interpret than the In-filtered or LiF-filtered data, because there was significant overlap of the third-order 517–613 Å spectrum with the second-order 775–920 Å spectrum. This was treated by using the In-filtered data to define the second-order response longward of 740 Å and the Sn-filtered data for the second-order response from 517 to 740 Å. From 407 to 517 Å the second-order efficiency was simply calculated from the theoretical grating efficiency, the SiC reflectivity, and the CsI quantum efficiency; the result was then normalized to match the measured efficiency longward of 517 Å. The third-order response for 517–615 Å could then be extracted from the region of overlap. Shortward of 517 Å the third-order efficiency was computed from the predicted component efficiencies and then scaled to match the measured values longward of 517 Å. Consistency checks could be performed by combining one of the Sn filters with either an In filter in the beam line or the Al filter mounted behind one of the slits in the spectrograph slit wheel, as either would modify the relative contributions of the different diffraction orders. The measured transmissions of the filters are shown in Figure 15.

The In and Sn filters produced data that were internally consistent and repeatable in the wavelength ranges mentioned above. The LiF filters were more troublesome. The LiF-filtered spectra had large undulations, with 30% modulation over wavelength scales of 100–200 Å. These undu-

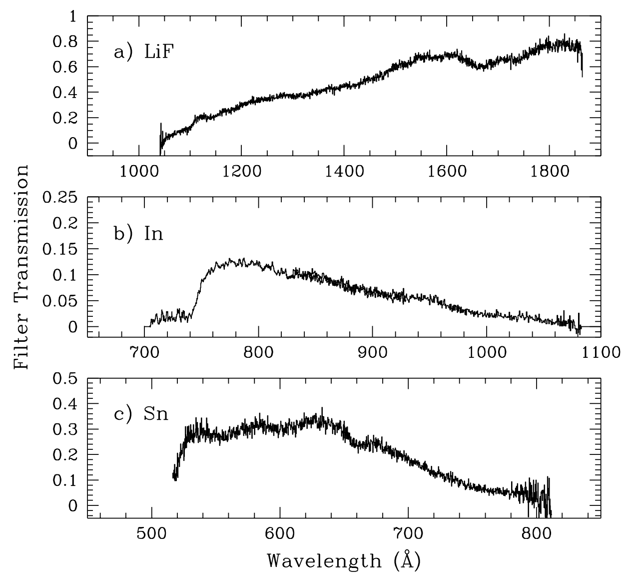

FIG. 15.—Measured transmissions of the filters employed for the preflight calibration measurements at SURF are plotted for (*a*) LiF, (*b*) In, (*c*) Sn. Regions that are noisy (because of negligible transmission) or unused (because of order overlap) have been omitted for clarity. The In filter transmission was measured in second order over 700–930 Å and in first order over 828–1070 Å. As can be seen, the agreement in the region of overlap is excellent.

lations varied from one run to the next and appeared to vary with even minute changes in the positions of the LiF filters relative to the beam axis. The suspicion is that the synchrotron beam itself (the intensity of which peaks at 100–200 Å) was creating color centers in the LiF crystals and altering the transmission of the filters. We took care to avoid exposing these filters to the full intensity of the synchrotron beam (which in normal operation is 5 orders of magnitude brighter than utilized for our measurements). We did not have sufficient beam time to explore this effect, so we simply combined a large number of LiF measurements in an attempt to average out fluctuations in the filter transmission. Although the resulting measurements are likely to contain substantial systematic errors, at most wavelengths they are consistent with the measurements obtained in the JHU calibration facility.

The effective area in each order was calculated as the product of the primary mirror area, its reflectivity, and the spectrograph efficiency. The results are shown in Figure 16. The smooth solid curves are the SURF measurements, and the plotted points with error bars are the JHU measurements. The dotted curve is the in-flight measurement of the first-order effective area. The in-flight measurements are in reasonable agreement with the preflight measurements at short wavelengths but fall well below them at longer wavelengths. This is consistent with our previous experience with aging of CsI photocathodes, which exhibit greater declines in quantum efficiency at longer wavelengths.

11. SENSITIVITY FOR EXTENDED SOURCES

All of the calibrations described in the previous sections are derived from observations of point sources. The astigmatism of the Rowland circle mount causes the image height of a point source to exceed the height of the detector diodes (2.5 mm) for wavelengths longward of ∼1770 Å for full and half-aperture observations. Approximately 2% of the incoming photons are lost at the extreme red end of the detector (1850 Å) for observations of a point source. This flux loss is absorbed into the definition of the instrument sensitivity for point sources. The size of the circular spectrograph slits used for point-source observations is small relative to the diode heights, so this loss is relatively insensitive to the position of the object within the slit (for most of the spectrum, no photons are lost no matter where the object is in the slit; at the long-wavelength end of the spectrum, photons lost from one tail of the point-spread function (PSF) for an object offset within the slit are partly compensated by photons from the other tail of the PSF that would ordinarily have fallen outside the diode but which now fall within it).

For observations of extended sources, however, the image height is a convolution of the astigmatic image height and the height of the slit. This causes a greater fraction of the incoming photons to be lost and shifts the onset of this effect to shorter wavelengths. The net result is that the shape of the effective area curve for extended sources differs from that for point sources and differs from one slit to another. Correction factors for this effect have been computed from ray traces of the telescope and spectrograph. These correction factors are shown plotted in Figure 17. These corrections are quite small for the circular apertures, being less than 1% at all wavelengths (usually much less). For the 10″ × 56″ slit, the corrections are still small, less than 1% shortward of 1700 Å and reaching a maximum value of ∼2% at 1850 Å. The 19″ × 197″ slit requires substantial corrections, however: 1% at 1100 Å, growing to 17% at the longest wavelengths. These curves flatten out or even roll over slightly at 1800 Å, because this is the wavelength at which the point-source throughput also begins to drop slightly.

Polynomial representations of these corrections have been computed, and the polynomial coefficients are given in Table 5. Fluxed spectra of extended sources that fill the spectrograph slits should be multiplied by the appropriate polynomial from this table. The automated data reduction process did not know a priori whether or not a given obser-

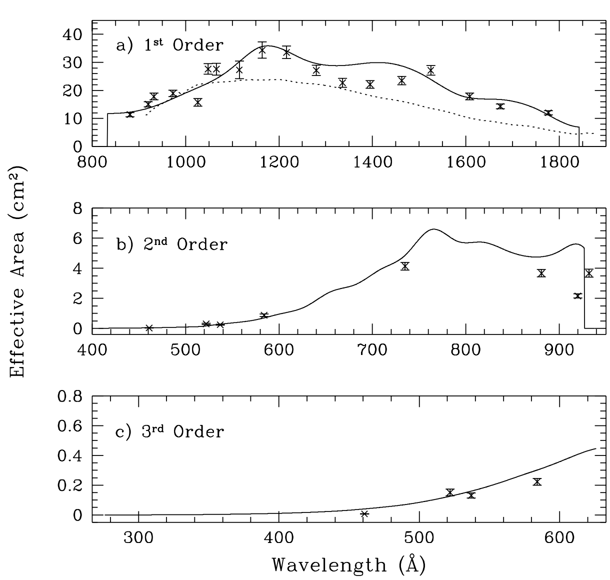

FIG. 16.—The preflight laboratory determinations of the instrument effective area are shown for (*a*) first order, (*b*) second order, and (*c*) third order. The solid smooth curves are the SURF measurements, and the single points are from the JHU calibration facility. The dotted curve in panel *a* is the in-flight measurement of the first-order effective area.

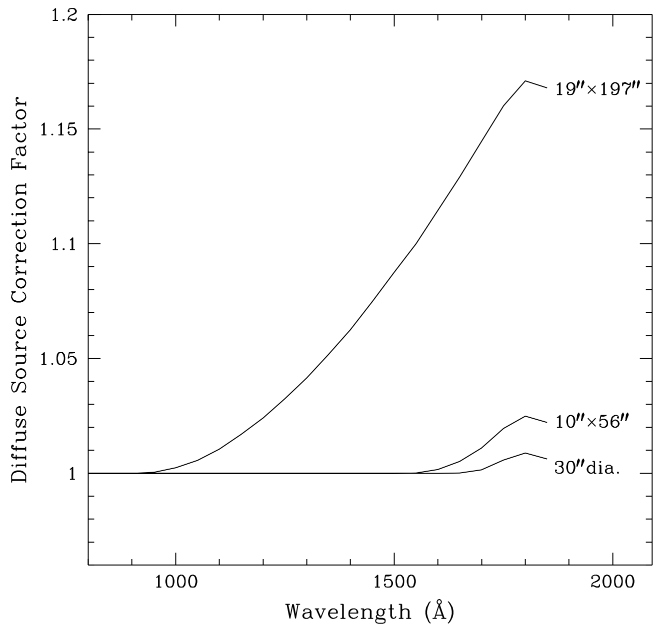

FIG. 17.—Correction factors for spectra of diffuse sources are plotted for the three largest spectrograph entrance slits. Spectra of sources that fill the slits should be multiplied by the corresponding curve.

vation was of an extended source; hence, this correction has not been applied to any of the archived spectra.

12. COMPARISON WITH THE PRELIMINARY CALIBRATION

The final full-aperture effective area shown plotted in Figure 8 is quite similar to the preliminary calibration presented by Kruk et al. (1995). Longward of 940 Å, the final effective area is 2% lower on average than that of the preliminary calibration, with rms deviations of less than 2%. Shortward of 940 Å, the final effective area rolls over more steeply, so that at the Lyman edge the new effective area is nearly 18% below that of the preliminary calibration. This difference is due in part to the lower value of $T_{\rm eff}$ used for the model of HZ 43 that defined the preliminary calibration (49,000 vs. 50,900 K) and in part to the fact that the improved treatment of the Stark broadening of the higher Lyman lines utilized in the new model results in lower overall opacity at these wavelengths.

The corrections for changes in effective area during the mission are quite similar to those presented in the preliminary calibration. The shapes of the curves are quite similar, but the magnitude of the correction at a given time is typically about 2% smaller than for the preliminary version over most of the wavelength range. At certain times the difference can be as great at 5%. The throughputs of the reduced aperture door configurations relative to the full aperture are essentially unchanged from the preliminary calibration.

13. INTERNAL CONSISTENCY OF THE CALIBRATION

Model atmosphere predictions for the star G191-B2B were tested directly against laboratory standards by Kruk et al. (1997) and were found to be consistent within the uncertainties of the lab calibration (4%–7%, depending on the wavelength scale examined). The improved sensitivity of HUT for Astro-2 required the use of different stars for the full-aperture calibration, however, and no postflight laboratory calibration was performed. The model atmosphere code used for the present work was one of the two codes tested by Kruk et al. (1997), so the main uncertainty in the definition of the Astro-2 full-aperture calibration is in the model parameters employed. The use of three stars to determine this calibration greatly reduces the probability that the accuracy of the calibration is affected by systematic errors in the determination of the model parameters for any single star. The wide range of effective temperatures for the stars chosen drastically changes the profiles of the Lyman lines and the strength of the "Lyman jump." The internal consistency of the calibration under these circumstances provides a stringent test of the accuracy of the adopted calibration and of the predictive ability of the model atmosphere codes.

The ratios of the individual measurements of the effective area to the final adopted calibration (the spline fit to the combined measurement) are shown in Figure 18. The internal consistency of the individual measurements can be examined on three different scales: the mean value over the entire spectrum, the gross spectral shape, and small-scale fluctuations.

The mean values of the ratios are 0.994, 1.023, and 1.022 for HZ 43, GD 71, and GD 153, respectively, indicating that the normalizations of the models are internally consistent to within 2%. Since the models are normalized at 5490 Å and fluxes at, say, 1150 Å vary relative to 5490 Å by 1% for a change in $T_{\rm eff}$ of $\sim$300 at 33,000 K or $\sim$700 at 50,000 K, the 2% consistency of the mean values of the effective area ratios implies that the effective temperatures are consistent within roughly 600 K for the two cooler stars and 1400 K for HZ 43. This does not imply that the effective temperatures are accurate to this degree, but only that within these limits the models share a common offset from the

TABLE 5

EXTENDED SOURCE FLUX CORRECTION POLYNOMIALS[a]

Coefficient	10″ × 56″	19″ × 197″
A_0	29.98486	17.08993
A_1	-1.730949×10^{-1}	-9.942307×10^{-2}
A_2	4.371819×10^{-4}	2.600641×10^{-4}
A_3	-6.052930×10^{-7}	-3.726892×10^{-7}
A_4	4.961271×10^{-10}	3.155845×10^{-10}
A_5	$-2.407308 \times 10^{-13}$	$-1.577997 \times 10^{-13}$
A_6	6.402509×10^{-17}	4.316143×10^{-17}
A_7	$-7.199998 \times 10^{-21}$	$-4.985230 \times 10^{-21}$

[a] Multiply spectrum by $A_0 + A_1\lambda + A_2\lambda^2 + \ldots + A_7\lambda^7$; λ in Å.

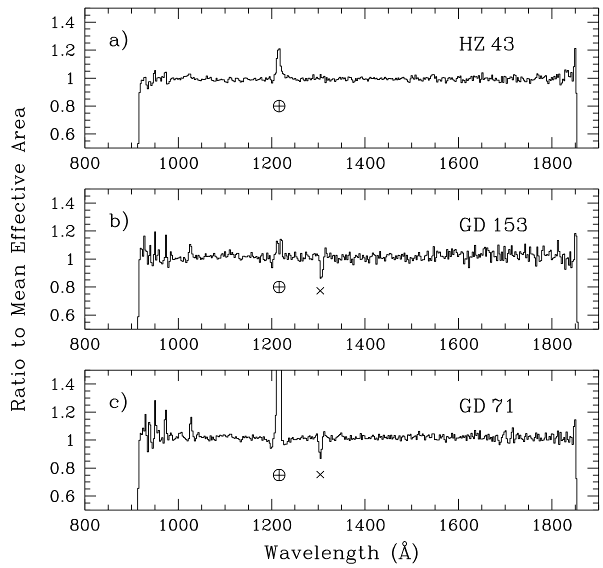

FIG. 18.—Ratios of the individual measurements of the effective area to the adopted calibration shown in Fig. 8 are plotted: (*a*) the ratio for the combined HZ 43 observations, (*b*) the GD 153 observation, (*c*) the GD 71 observation. The ratios have been binned by 5 pixels (roughly one resolution element) for plotting purposes.

"true" effective temperatures. The absolute normalizations of these models were determined in the same manner as for G191-B2B, which was shown to be consistent with laboratory standards within the measurement uncertainties of 4% (Kruk et al. 1997).

Tighter constraints on the consistency of the effective temperatures can be obtained from the fact that the ratios of the effective areas to the mean are flat, showing no end-to-end slope or significant undulations despite the fact that the stellar fluxes have quite different distributions over the HUT bandpass. Longward of 1100 Å, the flux is dominated by the Rayleigh-Jeans tail of the black-body distribution, so that the flux ratio F_λ(1100 Å)/F_λ(1800 Å) increases by only 7.5% as $T_{\rm eff}$ increases from 32,000 to 50,000 K. However, the Lyman jump strength, which we characterize by the ratio F_λ(920 Å)/F_λ(1100 Å), increases from 0.065 to 0.469 over the same temperature range. The flux at 920 Å provides a measure of the Lyman continuum flux, because the effective Lyman edge in the high-gravity atmosphere of a white dwarf is shifted to roughly 930 Å due to dissolution of the upper levels in the H atom by pressure ionization, while 1100 Å provides a reasonable sample of the blue end of the Balmer continuum flux that is unaffected by Lyman line absorption at the values of $T_{\rm eff}$ of interest here. The measured and predicted values of the flux ratios are given in Table 6. They generally match to within about 1% with the exception of GD 153, for which the measured value of F_λ(920 Å)/F_λ(1100 Å) exceeds the predicted value by 4%. The 4% discrepancy for GD 153 corresponds to an error in the effective temperature of 400 K, roughly equivalent to the 1 σ uncertainty for the value derived from Balmer line fitting.

On a pixel-by-pixel basis, the ratios of the individual measurements of the effective area to the final fitted effective area show rms deviations from unity of 1.7%, 2.0%, and 3.2% for HZ 43, GD 71, and GD 153, respectively, with the exception of 5 Å wide regions at the cores of the Lyman lines. At the cores of the Lyman lines all of the ratios show peaks, some as high as 15%–20%. The model line depths depend primarily on the effective temperature. However, the 1 σ uncertainties in the effective temperature correspond to only a 2%–3% change in the Lyman line depths, which rules out effective temperature errors as a possible cause of the discrepancy. If the width of the instrumental resolution used to smooth the model fluxes were increased by about 30%, a much better match to the observed profiles would be obtained. The instrumental resolution function used to smooth the model atmosphere spectra was the one presented as part of the preliminary calibration by Kruk et al. (1995). The considerably more detailed analysis of the spectral resolution presented in § 15 demonstrates that the actual instrumental resolution function for these observations was narrower than the preliminary resolution function, not broader. Another potential source for the excess flux in the line cores is grating scattering. A preliminary scattering profile was derived from fits to airglow lines and convolved with the model spectrum, resulting in an increase in the flux at the cores of the lines of about 4%. We also investigated whether non-LTE (NLTE) effects could alter the line profiles, using LTE and NLTE models kindly provided by Ivan Hubeny. NLTE effects are known to produce emission reversals in the cores of Balmer lines in hot DA white dwarfs. However, the only effect of NLTE on the Lyman lines is to slightly deepen the line cores: at the spectral resolution of HUT a typical result for a 50,000 K model is to deepen the line by 2% at its center, and the profile is unaffected beyond one resolution width from line center. These and other possible contributions to the excess flux in the line cores will be pursued further in future work.

The spline fit to the combined effective area measurements was constructed so as not to follow apparent features coinciding with the positions of the Lyman lines, because these are far more likely to be caused by errors in model parameters or uncertainties in the instrumental resolution function than to be indicative of the true instrument response. However, because the Lyman lines are quite broad, it is possible that the final effective area curve contains subtle broad systematic errors in the vicinity of the Lyman lines. To the extent that such errors are common to the models of all three stars, they would not appear in the ratios of the individual measurements to the final fit. To test for such errors we constructed a 10 term Legendre poly-

TABLE 6

WHITE DWARF SPECTRAL SHAPE

	F_λ(920 Å)/F_λ(1100 Å)		F_λ(1100 Å)/F_λ(1800 Å)	
STAR	Predicted	Measured	Predicted	Measured
HZ 43	0.447	0.446	5.160	5.113
GD 71	0.081	0.081	4.795	4.844
GD 153	0.215	0.224	4.886	4.824

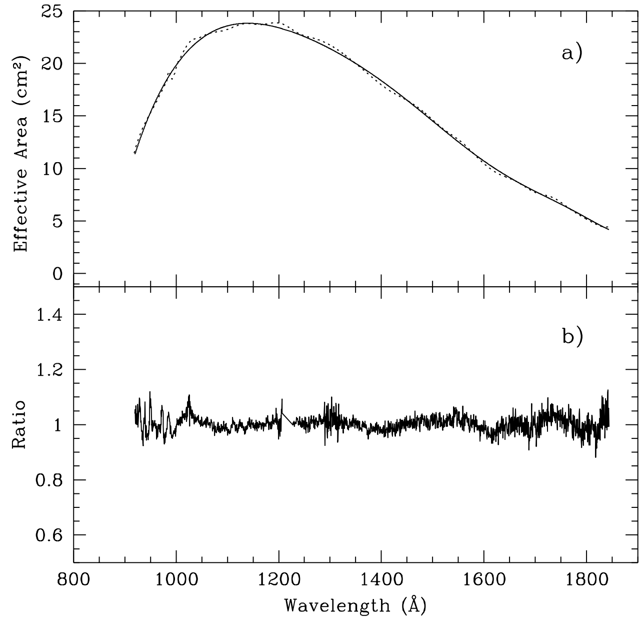

FIG. 19.—Panel *a* shows the adopted calibration of the full-aperture effective area as the dotted line and a 10 term Legendre polynomial fit to the data as the solid line. Panel *b* shows the ratio of the data to the fit. The rms deviations are only 1.6% and are not correlated with the positions of the Lyman lines, with the exception of a broad bump at Lyβ.

nomial fit to the measured effective area over the wavelength range 917–1830 Å. This polynomial fit follows the adopted effective area calibration well, as can be seen in Figure 19*a*. The residuals, shown in Figure 19*b*, are seen to be small, with an rms deviation from unity of 1.6%. The largest departure, at the few percent level, is at the "flat-field" feature at 992 Å. Shortward of 1000 Å, the effective area curve is seen to vary smoothly and does not correlate at all with the Lyman line positions. There is a small bump in the vicinity of Lyman α, with a peak value of 1.4% and FWHM of $\sim$30 Å, but the peak is at $\sim$1204 Å, significantly offset from the line center at 1216 Å. Therefore, we do not think there are model-dependent effects on the effective area calibration in the vicinity of Lyα. The remaining significant feature in the residuals is the bump near Lyβ, which has an amplitude of 2.8%, a width of about 30 Å, and is centered 2 Å longward of the center of Lyman β. Thus, the position and the width of the feature do appear to correlate with the Lyβ line. However, the character of this feature is similar to the other features in the residuals and may not be caused by an error in the calibration.

14. WAVELENGTH CALIBRATION

The HUT wavelength scale is determined simply by the relative placement of the spectrograph slit, grating, and detector, the grating equation, and the size of the detector pixels. It is insensitive to the aperture door configuration and to the position of the primary mirror. The in-flight changes in primary mirror focus position of 100 μm would change the plate scale at the detector by about half a pixel out of the 2000 spectral pixels. The spectrograph housing and grating substrate are fabricated from the same stainless steel alloy, so that the spectrograph focus and alignment is insensitive to changes in the overall temperature; thermal gradients were controlled to less than 1°C across the housing by a four-zone thermal control system. The axis of the slit wheel is in the dispersion plane, so that any potential errors in the slit wheel motions are transverse to the dispersion plane and leave the slit at a fixed entrance angle. Since the slits are larger than the primary mirror PSF, the main uncertainty in the wavelength scale arises from offsets of the star from the center of the slit. This can cause a shift in the zero point of the spectrum of up to a few pixels but does not affect the relative wavelengths.

The wavelength scale was calibrated by observations of the symbiotic stars AX Per, V1016 Cyg, RR Tel, EG And, Z And, and AG Dra. The emission-line spectra of these stars were fitted using the program SPECFIT (Kriss 1994); the fits are described in the following section. We found that the wavelength scale deviated from linearity by as much as 1.5 Å and that a four-term Legendre polynomial was required to reduce the residuals to half of a pixel or less. The resulting polynomial is

$$\lambda_i = 1344.813 P_0(x_i) + 530.9526 P_1(x_i) + 1.790137 P_2(x_i) - 0.3046105 P_3(x_i) ,$$

where λ_i is the wavelength of pixel i in Å, $x_i = (i - 1024.5)/1023.5$ and i ranges from 1 to 2048.

15. SPECTRAL RESOLUTION

The HUT spectral resolution is determined by four factors: the primary mirror PSF, the Spacelab pointing stability, the spectrograph optics, and the detector resolution. For point sources, the slit dimensions were significantly larger than the primary mirror PSF and were therefore not an important consideration. For extended sources the spectral resolution was usually limited by the slit dimensions. The pointing stability was often good enough to be a negligible contribution, unlike Astro-1, and usually could be corrected by software when it was significant, so it will not be discussed further here.

The width of the primary mirror PSF in the dispersion direction is the same for the four largest door configurations; for the 50 cm^2 door configuration the PSF width will probably be much smaller (see the discussion at the end of § 2.1 above). The width of the PSF produced by the primary mirror can be estimated from the program that computed photometric corrections from correlations of pointing errors with observed count rates. The width of the PSF at the slit was an input parameter to this program, which was allowed to vary freely in the preliminary data reductions. The resulting width was typically about 4″ FWHM (for a detailed discussion of this program, see Appendix A of Kruk et al. 1997). This width is an upper limit to the actual PSF produced by the primary mirror, because the spot size at the slit will be larger if the focal point is displaced from the slit surface along the optic axis. An image width of 4″ at the slit corresponds to a width at the detector of 35 μm, or about 1.5 Å.

The detector resolution is independent of door configuration and mirror position and is independent of position on the detector (i.e., independent of wavelength). It is estimated to be about 20 μm, or just over 1.5 pixels. If this is convolved with the primary mirror PSF of 4″, the result is an FWHM of 40 μm, or about 1.7 Å.

The dominant feature of the spectrograph optics is the mismatch of the flat detector and the curved focal surface. At the positions where the detector crosses the Rowland circle, the transverse aberrations go to zero (except for a high-order coma term) and the spectral resolution is limited by the detector resolution and the PSF of the primary mirror. However, away from these two points the line spread function (LSF) grows as the transverse *f*/number, which is determined by the aperture door configuration. For all but the 50 cm^2 door, the defocus grows as *f*/2. For the 200 and 750 cm^2 door configurations the defocusing away from the Rowland circle is effectively worse than *f*/2, because much of the core of the LSF has been obstructed by the combination of the narrow door opening and the obscuration of the center of the mirror by the spectrograph. The spectrograph focus is also quite sensitive to the primary mirror position. As the mirror focus is adjusted the grating focal surface moves closer or further from the diffraction grating, shifting the points at which the focal surface intersects the detector.

The spectral resolution was measured from the spectra of the symbiotic stars listed above in § 14 and from spectra of the coronal star α Aur. These stars have strong emission lines that are much narrower than the HUT spectral resolution and are thus well suited for measuring the HUT LSF in relatively brief exposures. The α Aur observation occurred during instrument activation and consisted of a series of short exposures as the focus of the primary mirror was varied in 50 μm steps over the range of -250 to $+250$ μm with respect to the preflight best-focus position. Pointing difficulties resulted in unusable data at the -100, -200, and -250 μm positions.

Symbiotic star data were obtained at focus offsets of ± 50 μm as well as at the two frequently used focus offsets of 0 and -100 μm, and one pointing (RR Tel) provided data for the 750 cm^2 door opening. No such data were available for the 50 cm^2 opening; however, given the low (*f*/23) divergence of the resulting light beam, it is reasonable to assume that the spectral resolution is determined solely by the primary mirror PSF and the detector resolution. This implies that it will be independent of wavelength and equal to the best resolution obtained through the full-aperture door, about 1.8 Å. It may in fact be somewhat better, because the image quality produced by the small illuminated portion of the mirror will likely be better than that of the entire mirror.

The width of the LSF as a function of wavelength was determined by fitting the emission lines with Gaussian profiles. For lines with sufficient S/N, a weak ($\sim 10\%$) broad component was added to the narrow component. This broad component was clearly seen in higher resolution spectra of the same stars obtained with the *HST* Goddard High Resolution Spectrograph (GHRS) and the Orbiting Retrievable Far and Extreme Ultraviolet Spectrograph (ORFEUS). The ORFEUS-I spectra for α Aur and for RR Tel used here were kindly provided by Mark Hurwitz of the ORFEUS instrument team. (A description of the Berkeley spectrometer on ORFEUS and its performance during the ORFEUS-I mission can be found in Hurwitz & Bowyer 1995, 1996, and references therein.) The narrow emission components are either unresolved in these high-resolution spectra or are demonstrated to be much narrower than the HUT instrumental resolution width. The underlying continuum was treated in a number of ways. For α Aur, the continuum was fitted with the tail of a very broad offset Gaussian component to mimic the rise of the G1 III stellar continuum, plus a localized linear component. For CH Cyg and RR Tel, a linear continuum was fitted in the vicinity of each line. For Z And, EG And, and AG Dra, the underlying continuum was modeled by a blackbody with atomic and molecular absorption and interstellar reddening. Details of the continuum fitting and treatment of interstellar absorption can be found in Birriel, Espey, & Schulte-Ladbeck (1998, 1999) for Z And EG And and in Espey & Schulte-Ladbeck (1999) for AG Dra.

In several instances the lines being fit are members of multiplets that are unresolved at HUT resolution, so we made use of high-resolution data to constrain the fits where possible. For α Aur, line fluxes from Linsky et al. (1995) were used to fix the multiplet ratios of Si IV, O IV/S IV, and C IV. Similarly, ORFEUS-I spectra were fitted by one of us (B. R. E.) to obtain relative intensities for deblending the O I 989 Å and N III 991 Å lines. The O VI 1032 Å, 1038 Å line ratio was found to be different in the HUT spectrum than in the ORFEUS-I spectrum, perhaps because of differences in orbital phase. Comparisons with GHRS data for the C III 1176 Å and C I 1656 Å multiplets were used to extract the effective HUT resolution at these wavelengths. For RR Tel, GHRS spectra were used to fix relative line intensities for the Si IV + O IV] blend and for the Mg VI] 1190 Å doublet, and ORFEUS-I data were used for the Ne VI] + N III blend. Additional information on these and the other fits can be found in Birriel, Espey, & Schulte-Ladbeck (1999) and Espey & Schulte-Ladbeck (1999).

The results of the fits are shown in Figure 20 for the full-aperture door at a mirror offset of 0 μm, Figure 21 for full-aperture door at a mirror offset of -100 μm, and Figure 22 for the 750 cm^2 door at a mirror offset of -100 μm. For any given wavelength the line widths generally varied as expected when the mirror focus position was changed. The only exception was the α Aur data at a focus offset of 0 μm, for which it was found that every line was

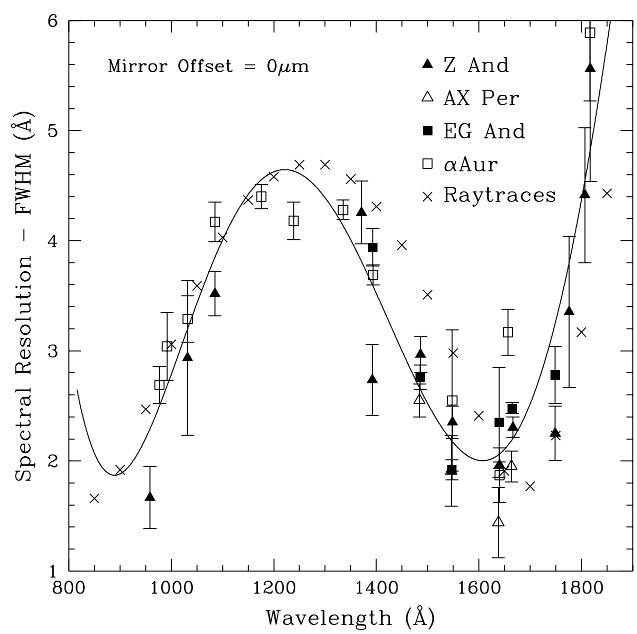

FIG. 20.—Spectral resolution is plotted for HUT configured with the door configuration set to full or half aperture and with the primary mirror at its nominal preflight focus position. The measured data are shown by the symbols with error bars, as labeled on the plot. The crosses represent the results of the ray trace simulations of the instrument, assuming the detector was bowed outward by 200 μm (see text). The smooth curve is a polynomial fit to the data.

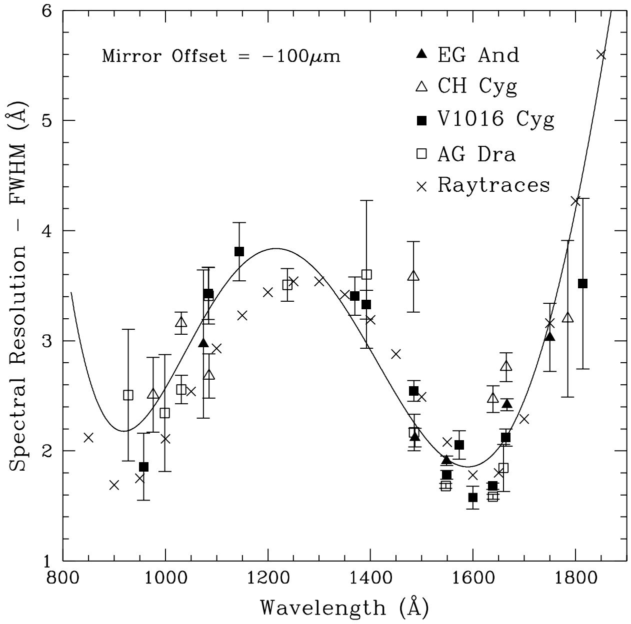

FIG. 21.—Spectral resolution is plotted for HUT configured with the door configuration set to full or half aperture and with the primary mirror offset from its nominal preflight focus position by −100 μm. The measured data are shown by the symbols with error bars, as labeled on the plot. The crosses represent the results of the ray trace simulations of the instrument, assuming the detector was bowed outward by 200 μm (see text). The smooth curve is a polynomial fit to the data.

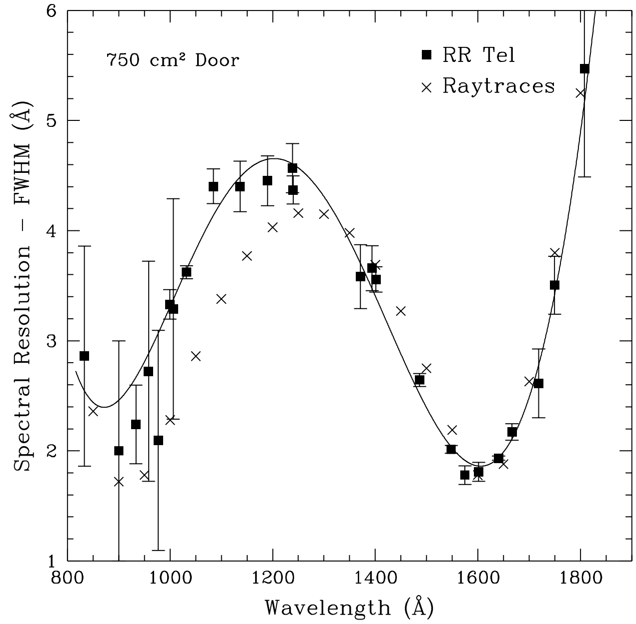

FIG. 22.—Spectral resolution is plotted for HUT configured with the door configuration set to 750 or 200 cm^2 and with the primary mirror offset from its nominal preflight focus position by −100 μm. The measured data are shown by the filled squares, as labeled on the plot. The crosses represent the results of the ray trace simulations of the instrument, assuming the detector was bowed outward by 200 μm (see text). The smooth curve is a polynomial fit to the data.

about 0.5 Å broader than would be expected relative to the α Aur data obtained at the other mirror positions. This is attributed to pointing jitter during that particular exposure, but because no pointing data were available in the telemetry for that observation, no correction was applied to the line widths. The solid curve shown in each figure is a six-term Legendre polynomial fit to the data. The values of the coefficients for these fits are given in Table 7. No measurements are available for the 750 cm^2 door opening at a mirror offset of 0 μm, but it would be reasonable to assume that it would be the same as for the offset of −100 μm at the minima and perhaps as much as 1 Å worse at the maxima. The resolution for the 200 cm^2 door opening should be the same as for the 750 cm^2 opening. The resolution for the 50 cm^2 opening should be roughly 1.8 Å at all wavelengths.

Each set of data shows pronounced minima at the points where the detector crosses the Rowland circle. The locations of these minima were initially interpreted (Kruk et al. 1995) as an indication that some component had shifted in a manner equivalent to moving the primary mirror 200 μm closer to the spectrograph relative to the preflight best-focus position. Ray traces of the instrument assuming a flat detector do provide the best match to the data obtained at a mirror offset of 0 μm if the detector is offset by 200 μm from its nominal position. However, these ray traces also predict that the resolution should have been 0.5–1 Å better than observed across the broad maximum at 1100–1300 Å for a mirror offset of −100 μm. In addition, ray traces with a flat detector cannot simultaneously fit the locations of the minima in the three sets of data shown. A much better match to the observed line widths is obtained in the ray traces if the MCPs are treated as being bowed outward by 200 μm at their center and the mirror is displaced 50 μm farther from the spectrograph than nominal. The resulting ray trace results are shown as the crosses in Figures 20, 21, and 22. The ray traces assume that the primary mirror pro-

TABLE 7

HUT SPECTRAL RESOLUTION FITS FOR DIFFERENT DOOR/MIRROR CONFIGURATIONS[a]

	DOOR: 5120 cm^2, 2560 cm^2		DOOR: 750 cm^2, 200 cm^2
COEFFICIENT	$\Delta = 0$ μm[b]	$\Delta = -100$ μm[b]	$\Delta = -100$ μm[b]
A_0	3.32306	3.01396	3.50235
A_1	0.43367	0.32441	0.35725
A_2	−0.27121	0.39978	0.33637
A_3	2.36581	1.78137	2.86663
A_4	1.60896	1.41518	1.67110
A_5	−0.78812	−0.72036	−0.43972

[a] FWHM(Å) = $\sum_{i=0}^{5} A_i P_i(x)$, x = (pixel − 1024.5)/1023.5.

[b] Mirror offsets (Δ) are relative to preflight focus position

duces a Gaussian spot with an FWHM of 4″ and that the detector resolution is 20 μm. The ray traces do a good job of reproducing the observed resolution and would be further improved if the "warping" of the MCPs was offset slightly from the center and if the surface of the plates were treated as being flat near the edges (where they are clamped) rather than being bowed spherically. Bowing the MCPs outward by 200 μm in the ray traces also serves to introduce nonlinearities in the wavelength scale that have a wavelength dependence similar to that seen in the data but with a somewhat smaller magnitude. In addition, the physical positions of the emission lines on the detector generally match the preflight measurements to within 1 pixel (12.5 μm, or 0.51 Å), which is easier to understand if the change in spectrograph focus was caused by a bowing of the MCPs rather than a displacement of an optical component by 200 μm.

The instrumental resolution function presented as part of the preliminary calibration by Kruk et al. (1995) was derived primarily from the spectrum of RR Tel and hence is essentially the same as that presented here for the 750 cm^2 door. A comparison of Figures 20, 21, and 22 shows that the preliminary resolution function is a reasonable representation of the spectral resolution for full-aperture observations obtained with the primary mirror at its nominal preflight position, but that it is too broad for the full-aperture observations obtained with the primary mirror offset by -100 μm.

The spectral resolution for observations of extended sources can be obtained by convolving the above results with the slit width. Nominal values for the effective slit widths are: 12″ diameter, 3.1 Å; 20″ diameter, 5.1 Å; 30″ diameter 7.7 Å; 10″ × 56″, 3.6 Å; 19″ × 197″, 6.9 Å. In practice, the resolution obtained was slightly better than this.

16. DATA REDUCTION PROCEDURE FOR ARCHIVED HUT DATA

The data reduction procedures applied to the HUT spectra archived in the NSSDC are in most respects identical to those described above in § 3.1. There are two significant differences: (1) no airglow subtraction is attempted and (2) no corrections for second-order or third-order EUV flux are applied. The individual steps in the reduction procedure for the archived data are listed here for completeness; the comments pertaining to each step given in § 3.1 apply here as well:

1. Accumulate the spectrum between the designated start and stop times, with and without correcting for pointing jitter. Compute a photometric correction by fitting the slit throughput function to pointing errors and observed count rates.
2. Correct for detector dead time.
3. Correct for phosphor persistence effects.
4. Subtract dark count.
5. Apply the flat-field correction.
6. Subtract scattered light. This also serves to correct for any additional background induced by SAA passages.
7. Subtract second-order FUV (>912 Å) counts.
8. Divide by exposure time.
9. Multiply by the inverse sensitivity curve to obtain the fluxed spectrum.
10. Multiply by the photometric correction calculated in step 1.

Some general comments concerning the reduction of the archived data are in order:

1. Each processed spectrum is written as a FITS file, with a record of all processing written into the header.
2. The start and stop times for an exposure include the entire time that the instrument was in a well-defined configuration (slit in place, aperture doors opened to the designated position, primary mirror motions complete, etc.). In general, this start time does not coincide with the entrance of the target into the spectrograph slit. If the target acquisition was performed with the desired slit already in place, there will probably be several hundred seconds of airglow included in the exposure. The photometric correction procedure will generally scale the flux properly to account for the fact that the nominal exposure time is greater than the time the target spent in the slit. For example, consider a 500 s target acquisition followed by a 1000 s exposure. The apparent exposure time is 1500 s, and the photometric correction procedure will multiply the counts in the spectrum by 1.5. When the spectrum is converted to flux units, the source flux will be correct. In principle, it would have been possible to develop an algorithm that would have excluded the airglow-only telemetry frames. However, it would have been difficult to ensure that such an algorithm would handle faint sources or erratic pointing without inadvertently discarding much of the real data. The advantages of the adopted approach are that full use is made of data obtained while the source was in the slit prior to the BEGIN command (often several hundred seconds) and accurate source fluxes are obtained even if the source is on the edge of the slit for much of the observation. The disadvantages are that the total airglow contamination is greater than if the data obtained prior to the BEGIN were simply discarded and that the fluxes reported for the airglow emissions are too large by a factor equal to the applied photometric correction.
3. If an exposure spans a terminator crossing, it is processed 3 times: (a) the entire exposure, (b) the night side portion of the exposure, and (c) the day side portion of the exposure.
4. Each spectrum was accumulated with and without corrections for pointing jitter. The corrected and uncorrected spectra were separately processed and both are included in the archive.
5. The photometric correction factor is potentially unreliable for extended sources such as nebulae, supernova remnants, and planets, because the count rate will not necessarily be correlated with the error in the pointing position. It may also be unreliable for point sources that are so faint that the signal is comparable to (or smaller than) the background rate. The user should examine the FITS header in such cases to see if this correction was applied and decide whether or not to renormalize the spectrum accordingly.
6. The wavelength calibration inserted into the FITS header is not adjusted for any possible zero-point shifts. The user may need to shift each spectrum by up to a few pixels to obtain accurate wavelengths.

17. SUMMARY

We have described the essential characteristics of the HUT instrument and those aspects of mission operations affecting data quality in order to maximize the utility of the archived HUT data. Instrument configurations requiring specific calibrations were identified and the calibrations described. Uncertainties in the calibrations were identified whenever possible.

The sensitivity calibration of HUT was defined by model atmosphere predictions for the flux of the hot DA white dwarfs HZ 43, GD 153, GD 71, and G191-B2B. The parameters of the models were determined previously by fits to Balmer line profiles, and the models were normalized by the observed *V* magnitudes. The first three stars were observed through the full-aperture door and gave results that were consistent with one another to better than 3% at all wavelengths outside the cores of the Lyman lines.

The calibration of the full-aperture sensitivity was extended to the other aperture door configurations by observing suitable stars through multiple door configurations. The result for the smallest (50 cm^2) door was then tested by comparing the HUT spectrum of BD $+75°325$ obtained through this door with the FOS spectrum of this star; the two spectra differed by no more than 5% in the region of overlap.

The sensitivity was found to decrease over the first 229 hours of the mission. The total decline was only 5% at 1840 Å but increased smoothly with decreasing wavelength to a maximum of 26% at 912 Å. This loss of sensitivity has been tentatively ascribed to contamination of the primary mirror by materials in the shuttle environment.

A number of "flat-field" features were found, all of which were apparently caused by exposure of the detector to intense localized emission features. Preflight calibration work induced four such features, which remained constant in strength throughout the mission. Observations of the Wolf-Rayet star HD 50896 created three such features at the locations of the brightest emission lines: N v 1240 Å, C iv 1550 Å, and He ii 1640 Å. The strength of these three features increased following each of the observations of this star. Airglow emission caused three additional features: a weak feature at 989 Å and two very strong features at Lyα and 1304 Å. All features other than those at Lyα and 1304 Å are corrected in the data reduction process. The corrections for full and half-aperture observations are fairly well characterized, but the corrections for the HD 50896–induced features in the smaller door configurations seem to be variable (probably depending on the exact position of the spectrum on the photocathode), and the data reduction process may undercorrect these features by as much as a factor of 2 in any given observation.

The preflight calibration of the instrument sensitivity in second and third order is given. The reflective coatings used for this mission resulted in significantly lower second- and third-order sensitivity relative to the Astro-1 instrument. These sensitivities are of interest primarily for the analysis of the DA spectra used here to define the calibration and possibly for analysis of the spectra of solar system objects.

Corrections to the instrument sensitivity for extended sources were defined. These corrections arise from a combination of the astigmatism of the Rowland grating mount and the height of the spectrograph slits, causing photons to fall outside the active area of the detector. This effect is quite small (<3%), except for the $19'' \times 197''$ slit, for which it peaks at 17%. These corrections must be applied to the archived data by the user.

The wavelength scale and spectral resolution were determined by observations of symbiotic stars and the coronal star α Aur. The wavelength scale exhibited small nonlinearities, which are well described by a four-term Legendre polynomial. The spectral resolution for point sources varied with wavelength from 1.8 to 3.5 Å or 1.8 to 4.5 Å, depending on the door configuration and the position of the primary mirror. For observations through the 50 cm^2 door opening, the spectral resolution was estimated to be about 1.8 Å, independent of wavelength.

The excellent internal consistency of the full-aperture sensitivity calibration demonstrates the predictive power of the present white dwarf models for stars with pure hydrogen atmospheres. Impressive internal consistency of calibrations derived from synthetic white dwarf spectra has already been obtained at wavelengths longward of 1150 Å (Bohlin et al. 1995); however, the synthetic spectra are considerably more sensitive to small changes in the model parameters at wavelengths shortward of 1150 Å than at longer wavelengths. Demonstrating internal consistency down to the Lyman edge is an important extension of the Astro-1 HUT calibration, which demonstrated that a synthetic spectrum of G191-B2B and laboratory flux standards gave results consistent to within the uncertainties of the laboratory calibration (4%–7%). These new results imply that any pure hydrogen white dwarf with an effective temperature in the range of 32,000 to 61,000 K may be used as a primary flux standard in the far UV, so long as high-quality optical spectroscopy is available to derive model atmosphere parameters for the star and accurate photometry is available to normalize the model flux.

We would like to thank Mitch Furst and the staff at SURF for their assistance with the preflight calibration. We are grateful to Ritva Keski-Kuha and the Optics Branch at GSFC for providing measurements of our witness mirrors throughout the duration of the project and for providing a surface analysis of the flight witness mirrors. We would like to thank Ben Ballard and John Hayes for their work on the flight software enabling the use of partial door openings and for their analysis of the uncertainties in the door opening time. Finally, we would like to thank Mark Hurwitz for providing the ORFEUS spectra employed in the spectral resolution calibration. The Hopkins Ultraviolet Telescope Project is funded by NASA contract NAS 5-27000.

REFERENCES

Bergeron, P. 1993, in White Dwarfs: Advances in Observation and Theory, ed. M. Barstow (Dordrecht: Kluwer), 267
Birriel, J. J., Espey, B. R., & Schulte-Ladbeck, R. E. 1998, ApJ, 507, L75
———. 1999, in preparation
Bohlin, R. C. 1996, AJ, 111, 1743
Bohlin, R. C., Colina, L., & Finley, D. S. 1995, AJ, 110, 1316
Däppen, W., Anderson, L., & Mihalas, D. 1987, ApJ, 319, 195
Davidsen, A. F., et al. 1992, ApJ, 392, 264
Dupuis, J., Vennes, S., Bowyer, S., Pradhan, A. K., & Thejll, P. 1995, ApJ, 455, 574
Espey, B. R., & Schulte-Ladbeck, R. E. 1999, in preparation
Finley, D. S., Kimble, R. A., Koester, D., & Kruk, J. W. 1999, in preparation
Finley, D. S., Koester, D., & Basri, G. 1997, ApJ, 488, 375 (FKB)
Hedin, A. E. 1987, J. Geophys. Res., 92, 4649
Hummer D. G., & Mihalas D. 1988, ApJ, 331, 794

Hurwitz, M., & Bowyer, S. 1995, ApJ, 446, 812
———. 1996, in IAU Colloq. 152, Astrophysics in the Extreme Ultraviolet, ed. S. Bowyer & R. F. Malina (Dordrecht: Kluwer), 601
Hurwitz, M., Jelinsky, P., & Dixon, W. V. D. 1997, ApJ, 481, L31
Kimble, R. A., et al. 1993a, ApJ, 404, 663
Kimble, R. A., Davidsen, A. F., Long, K. S., & Feldman, P. D. 1993b, ApJ, 408, L41
———. 1998, ApJ, 492, L83
Koester, D., Finley, D. S., Allard, N. F., Kruk, J. W., & Kimble, R. A. 1996, ApJ, 463, L93
Kortright, J. B., & Windt, D. L. 1988, Appl. Optics 27, 2841
Kriss, G. A. 1994, in ASP Conf. Proc. 61, Astronomical Data Analysis Software and Systems III, ed. D. R. Crabtree, R. J. Hanisch, & J. Barnes (San Francisco: ASP), 437
Kruk, J. W., Durrance, S. T., Kriss, G. A., Davidsen, A. F., Blair, W. P., Espey, B. R., & Finley, D. S. 1995, ApJ, 454, L1
Kruk, J. W., Kimble, R. A., Buss, R. H., Jr., Davidsen, A. F., Finley, D. S., Holberg, J. B., & Kriss, G. A. 1997, ApJ, 482, 564
Lemke, M. 1997, A&AS, 122, 285
Linsky, J. L., Wood, B. E., Judge, P., Brown, A., Andrulis, C., & Ayres, T. R. 1995, ApJ, 442, 381
Long, K. S., Bowers, C. W., Tennyson, P. D., & Davidsen, A. F. 1985, Adv. Electron. Electron Phys., 64A, 239
Mihalas, D., Däppen, W., & Hummer D. G. 1988, ApJ, 331, 815
Morton, D. C. 1991, ApJS, 77, 119
Nichols, J. S., & Linsky, J. L. 1996, AJ, 111, 517
Nordsieck, K. H., Code, A. D., Anderson, C. M., Meade, M. R., Babler, B., Michalski, D. E., Pfeifer, R. H., & Jones, T. E. 1994, Proc. SPIE, 2010, 2
Siegmund, O. H. W. 1989, Proc. SPIE, 1072, 111
Stecher, T. P., et al. 1997, PASP, 109, 584
Vidal, C. R., Cooper, J., & Smith, E. W. 1973, ApJS, 25, 37
Wiese, W. L., Kelleher, D. E., & Paquette, D. R. 1972, Phys. Rev. A, 6, 1132